

Broadband Electromechanical Diode: Acoustic Non-Reciprocity in Weakly Nonlinear Metamaterials With Electromechanical Resonators

Mohammad Bukhari

Department of Mechanical Engineering, Virginia Tech, Blacksburg, VA 24061 e-mail: bukhari@vt.edu

Oumar Barry¹

Department of Mechanical Engineering, Virginia Tech, Blacksburg, VA 24061 e-mail: obarry@vt.edu

Recent attention has been given to acoustic non-reciprocity in metamaterials with nonlinearity. However, the study of asymmetric wave propagation has been limited to mechanical diodes only. Prior works on electromechanical rectifiers or diodes using passive mechanisms are rare in the literature. This problem is investigated here by analytically and numerically studying a combination of nonlinear and linear metamaterials coupled with electromechanical resonators. The nonlinearity of the system stems from the chain in one case and from the electromechanical resonator in another. The method of multiple scales is used to obtain analytical expressions for the dispersion curves. Numerical examples show potential for wider operation range of electromechanical diode, considerable harvested power, and significant frequency shift. The observed frequency shift is demonstrated using spectro-spatial analyses and it is used to construct an electromechanical diode to guide the wave to propagate in one direction only. This only allows signal sensing for waves propagating in one direction and rejects signals in any other direction. The performance of this electromechanical diode is evaluated using the transmission ratio and the asymmetric ratio for a transient input signal. Design guidelines are provided to obtain the best electromechanical diode performance. The presented analyses show high asymmetry ratio for directional-biased wave propagation in the medium-wavelength limit for the case of nonlinear chain. Indeed, the present asymmetric and transmission ratios are higher than those reported in the literature for a mechanical diode. The operation frequencies can also be broadened to the long-wavelength limit frequencies using the resonator nonlinearity. [DOI: 10.1115/1.4054962]

Keywords: nonlinear vibration, nonlinear metamaterials, acoustics non-reciprocity, electromechanical diode

1 Introduction

Metamaterials are artificially fabricated in special engineering configurations and constitutions. These configurations enable interesting dynamical properties that cannot be found in conventional homogeneous materials [1,2]. These interesting unique properties make metamaterials perform incredibly in a wide pool of engineering applications (e.g., low-frequency vibration mitigation, directional-biased wave propagation, wave focusing, and cloaking).

Metamaterials can be arranged in periodic patterns of cells also known as phononic crystals [3–8]. Periodicity in phononic crystals can be represented by periodicity in material, geometry, and boundary conditions. These periodic crystals can reflect waves with a wavelength near the lattice constant due to Bragg scattering and hence they can be employed in low-frequency vibration reduction applications. Nevertheless, the restriction on the lattice constant size limits this application to large structures only.

In order to extend the application of metamaterials to control smaller structures, researchers suggested embedding local resonators inside the cells [9]. This breaks the size constraint in Bragg

scattering and allows hybridizing the resonance mode with the longwave nondispersive modes of the underlying medium, thus reflecting waves with wavelength much smaller than the lattice constant even in the absence of periodicity [10]. Indeed, both Bragg scattering and mode hybridization can be observed in locally resonant metamaterials; however, each effect can be dominant at certain design parameters [11].

In addition to these unique low-frequency vibration attenuation phenomena observed in linear metamaterials, nonlinearity in metamaterials can show further interesting wave propagation phenomena. This includes, but is not limited to, adjusted bandgap limits [12], solitons [13,14], directional-biased wave propagation [15], and enhanced energy harvesting and sensing [16].

These interesting nonlinear wave propagation phenomena can be obtained through different analytical and numerical analyses. For analytical analyses, the type and the strength of nonlinearity determine how the problem can be tackled. For instance, weakly nonlinear systems can be handled using different perturbation approaches [17,18]. The use of these techniques can be found in Ref. [19] for nonlinear chains, in Ref. [20] for locally resonant metamaterials, and in Ref. [21] for nonlinear chains with multiple linear and nonlinear local resonators. On the other hand, systems with strong nonlinearity should be handled using different techniques and closed form solution can be obtained in some cases analytically [22], or with the help of homotopy analyses [23]. However, numerical analyses should be employed when the approximate analytical solution

¹Corresponding author.

Contributed by the Noise Control and Acoustics Division of ASME for publication in the JOURNAL OF VIBRATION AND ACOUSTICS. Manuscript received April 6, 2022; final manuscript received June 29, 2022; published online October 19, 2022. Assoc. Editor: James Gibert.

of the problem is not accurate or when interesting nonlinear phenomena cannot be revealed by analytical analyses. These analyses include temporal space analyses and spectro-spatial analyses [20,21,24–26].

The bandgap size in locally resonant metamaterials depends significantly on the added mass to the system, in that a wider bandgap requires a larger mass. Therefore, controlling vibrations in the structure may be limited by weight restrictions in many engineering applications. These restrictions can be overcome by adding a stiffness to the structure through attaching piezoelectric patches to periodic patterns of cells [27-31]. In particular, electromechanical coupling can generate an electromechanical bandgap. The piezoelectric can also be used for energy harvesting and sensing. This is inspired by the flat frequency band in metamaterials and can be realized by shunting the piezoelectric material to a load resistor [32–36]. Consequently, metamaterials can be used for simultaneous energy harvesting and vibration reduction applications. For weak electromechanical coupling, it was analytically and experimentally shown that harvesting energy in metamaterials has no effect on the bandgap size [37]. The study of nonlinear systems also showed that the bandgap size is only affected by the nonlinearity in the chain in the case of weak electromechanical coupling.

Non-reciprocity in acoustic and elastic metamaterials can be obtained by breaking the time reversal symmetry [38]. Several techniques are presented in the literature to break the time reversal symmetry. For instance, kinetic media with moving parts or circulating flows can lead to acoustic non-reciprocity [39,40]. Additionally, varying material properties in activated media can lead to breaking the time reversal symmetry [41,42]. The modulation frequency and amplitude of the property variation in the time and space domains have a significant role in the obtained non-reciprocity. Examples in the literature discussed the low-frequency amplitude variation (i.e., one-way Bragg mirror) [43-45], large amplitude-fast modulation (i.e., Willis coupling) [46], slow modulation and topological properties (i.e., quantum Hall effect) [47,48], and piezoelectric metastructure shunted with one-way electric transmission lines [49]. The aforementioned techniques are limited by their impracticality and the need of applying external bias. Therefore, researchers have drawn their attention to other passive techniques by considering nonlinear metamaterials.

The nonlinearity in metamaterials can lead to a significant wave distortion. This wave distortion results in frequency conversion, enabling output waves to appear at frequencies different from the input wave frequency. Indeed, when the nonlinear metamaterial is coupled to a linear metamaterial (i.e., the linear metamaterial has a bandgap tuned to the frequency conversion region in the nonlinear metamaterial), the energy content with shifted frequency can propagate in the forward configuration. However, waves propagating from the linear metamaterial side (backward configuration) will be tuned inside the linear metamaterial's bandgap. This is an indication that directional-biased wave propagation can be realized [15,50–53]. This wave non-reciprocity can also be observed in nonlinear granular structures [52] or nonlinear hierarchical internal structures [54]. Spectro-spatial analyses can be employed to examine the frequency conversion in nonlinear metamaterials. The spectro-spatial features can show a significant frequency shift at the medium-wavelength limit in both nonlinear chain and nonlinear local resonators metamaterials [16,20,21]. Unlike the case of nonlinear chain, nonlinear local resonator metamaterials can also show significant frequency shift at the long-wavelength limit in addition to the medium-wavelength limit [21,55]. Models of acoustic diodes are limited to the use of local mechanical resonators embedded within the periodic structure or simple coupling between linear and nonlinear metamaterials. To the best of our knowledge, there are no works in the literature investigating the use of electromechanical resonators in nonlinear metamaterials for designing electromechanical diodes except our preliminary work, recently published in a conference proceeding [56]. In addition, there is no work in the literature that employs the benefit of frequency shift for the case of nonlinear resonator to broaden the operation frequency of the electromechanical diode. Consequently, the asymmetric and transmission ratios are not relatively high for diodes reported in the literature. Furthermore, design guidelines for broadening the operation range of mechanical/electromechanical diode and increasing the asymmetry ratio are rarely found in the literature. These knowledge gaps form the core motivation of the current study.

In this paper, we study how a weakly nonlinear metamaterial with electromechanical local resonators can be used to maximize the performance of electromechanical diodes (i.e., increase both asymmetry and transmission ratios). The nonlinearity stems from the chain in one case and from the local electromechanical resonator in another, and is of a cubic type. These sources of nonlinearities can offer different operation frequency regions for the diode. The former can enable the diode to operate at medium-wavelength limit, while the latter can broaden the operation frequency range since it can enable the diode to operate at both medium-/longwavelength limits. The system is simulated numerically and validated against other models in the literature. The numerical results are used to obtain the band structures and analyzed further by spectro-spatial analyses to demonstrate the frequency shift in the nonlinear proposed structure. This frequency shift is then used to design an electromechanical diode. The designed electromechanical diode is evaluated based on its transmission ratio and the asymmetric ratio for a transient input signal. The rest of the paper is as follows. In Sec. 2, we present a mathematical model for the proposed weakly nonlinear metamaterial and the linear and nonlinear dispersion relations. In Sec. 3, we present the analytical and numerical band structures for different types of nonlinearities. Then, the significant frequency shift observed by analyzing the spectro-spatial features is presented in Sec. 4. This significant frequency shift is employed to design an electromechanical diode in Sec. 5. In Sec. 6, design guidelines for best electromechanical diode performance are provided. Finally, we summarize the main findings in the conclusion section.

2 System Description and Mathematical Modeling

A schematic diagram for the metamaterial chain with electrome-chanical resonators is shown in Fig. 1. The chain is constructed of s periodic cells with a mass, M, lattice constant, a, and connected by a linear or weakly nonlinear spring. The springs have linear coefficient, K, and nonlinear coefficient, $\bar{\alpha}$. Attached to each cell, there is a local linear or nonlinear electromechanical resonator shunted to an external resistor R. The electromechanical resonator has effective mass, m_p , effective linear stiffness, k_1 , effective nonlinear stiffness, $\bar{\alpha}_r$, electromechanical coupling coefficient, θ , and capacitance of the piezoelectric element, C_p . It is noteworthy here that the system is reduced to a linear system when $\bar{\alpha}=0$ and $\bar{\alpha}_r=0$. Moreover, we set $\bar{\alpha}_r=0$ for the case of nonlinear chain only, while we set $\bar{\alpha}=0$ for the case of nonlinear resonator.

In the absence of damping, the equation of motions for the nth cell and its electromechanical resonator can be expressed as follows:

$$M\ddot{\bar{u}}_n + 2K\bar{u}_n - K\bar{u}_{n+1} - K\bar{u}_{n-1} + \bar{\alpha}(\bar{u}_n - \bar{u}_{n+1})^3 + \bar{\alpha}(\bar{u}_n - \bar{u}_{n-1})^3 + k_1(\bar{u}_n - Y_n) + \bar{\alpha}_r(\bar{u}_n - Y_n)^3 = 0$$
(1)

$$m_p \ddot{Y}_n + k_1 (Y_n - \bar{u}_n) + \bar{\alpha}_r (Y_n - \bar{u}_n)^3 - \theta \bar{v}_n = 0$$
 (2)

$$RC_p \dot{\bar{v}}_n + \bar{v}_n + R\theta(\dot{Y}_n - \dot{\bar{u}}_n) = 0 \tag{3}$$

where \bar{u}_n is the displacement of the *n*th cell, Y_n is the absolute displacement of the electromechanical resonator, \bar{v}_n is the harvested voltage in the *n*th electromechanical resonator, and the dots are

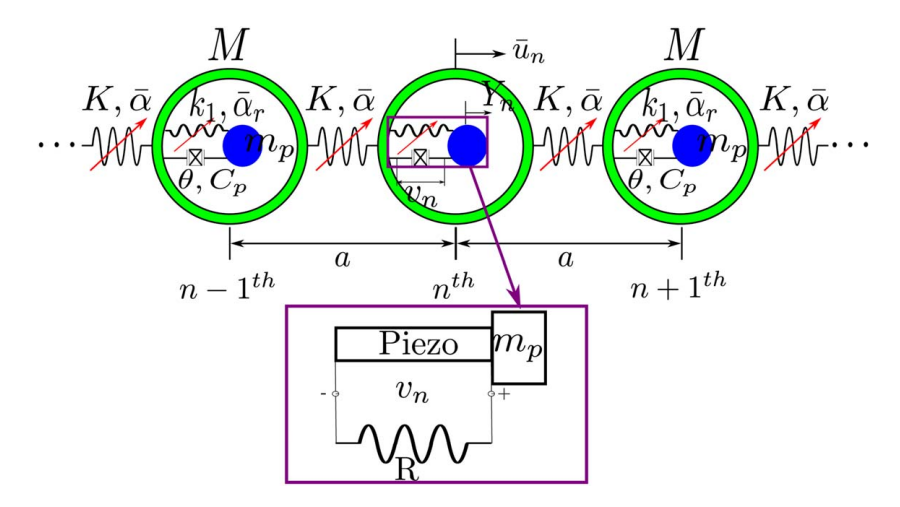


Fig. 1 A schematic diagram for the nonlinear acoustic metamaterial with electromechanical resonators

the derivative with respect to time. To get compact set of equations, we define the relative displacement of the nth electromechanical resonator as $\bar{y}_n = Y_n - \bar{u}_n$. Therefore, the governing equations of motion of the nth cell become

$$M\ddot{\bar{u}}_n + 2K\bar{u}_n - K\bar{u}_{n+1} - K\bar{u}_{n-1} + \bar{\alpha}(\bar{u}_n - \bar{u}_{n+1})^3 + \bar{\alpha}(\bar{u}_n - \bar{u}_{n-1})^3 + m_p(\ddot{\bar{y}}_n + \ddot{\bar{u}}_n) = 0$$
(4)

$$m_p \ddot{\bar{y}}_n + k_1 \bar{y}_n + \bar{\alpha}_r \bar{y}_n^3 - \theta \bar{v}_n = -m_p \ddot{\bar{u}}_n \tag{5}$$

$$RC_p \dot{\bar{v}}_n + \bar{v}_n + R\theta \dot{\bar{y}}_n = 0 \tag{6}$$

We introduce the following variables and parameters in order to normalize Eqs. (4)–(6):

$$\omega_{n}^{2} = K/M, \ \omega_{d}^{2} = k_{1}/m_{p}, \ \bar{k} = k_{1}/K, \ u_{n} = \bar{u}_{n}/U_{0}$$

$$y_{n} = \bar{y}_{n}/U_{0}, \ v_{n} = \bar{v}_{n}/V_{0}, \ \varepsilon\alpha = \bar{\alpha}U_{0}^{2}/K, \ \varepsilon\alpha_{r} = \bar{\alpha}_{r}U_{0}^{2}/k_{1}$$

$$\Omega_{0} = \omega_{n}/\omega_{d}, \ \alpha_{1} = \theta V_{0}/k_{1}, \ \alpha_{2} = RC_{p}\omega_{n}$$

$$\alpha_{3} = R\theta\omega_{n}y_{0}/V_{0}, \ \tau = \omega_{n}t$$
(7)

where U_0 and V_0 are the zeroth cell displacement amplitude and harvested voltage amplitude, respectively.

Substituting Eq. (7) into Eqs. (4)–(6) yields the following normalized equations:

$$\ddot{u}_n + 2u_n - u_{n+1} - u_{n-1} + \varepsilon \alpha (u_n - u_{n+1})^3 + \varepsilon \alpha (u_n - u_{n-1})^3 + \bar{k} \Omega_0^2 (\ddot{y}_n + \ddot{u}_n) = 0$$
(8)

$$\Omega_0^2 \ddot{y}_n + y_n + \varepsilon \alpha_r y_n^3 - \alpha_1 v_n = -\Omega_0^2 \ddot{u}_n \tag{9}$$

$$\alpha_2 \dot{v}_n + v_n + \alpha_3 \dot{y}_n = 0 \tag{10}$$

In order to obtain an approximate analytical solution, we need to expand the solution using the power series and separate the linear and nonlinear problems. To handle the problem using the method of multiple scales, we assume that the system is weakly nonlinear (i.e., $\alpha = \varepsilon \alpha$, and $\alpha_r = \varepsilon \alpha_r$). Therefore, the first-order expansion can be written as

$$u_n(t, \varepsilon) = u_{n0}(T_0, T_1) + \varepsilon u_{n1}(T_0, T_1) + o(\varepsilon^2)$$
 (11)

$$y_n(t, \varepsilon) = y_{n0}(T_0, T_1) + \varepsilon y_{n1}(T_0, T_1) + o(\varepsilon^2)$$
 (12)

$$v_n(t, \varepsilon) = v_{n0}(T_0, T_1) + \varepsilon v_{n1}(T_0, T_1) + o(\varepsilon^2)$$
 (13)

where $T_0 = \tau$ and $T_1 = \varepsilon \tau$ are the fast and slow time scales, respectively, while ε is a small dimensionless parameter.

In addition, the partial derivatives with respect to the defined time scales can be expressed using the chain rule as

$$(\dot{}) = D_0 + \varepsilon D_1 + \cdots \tag{14}$$

$$(") = D_0^2 + 2\varepsilon D_0 D_1 + \cdots$$
 (15)

Substituting Eqs. (11)–(15) into Eqs. (8)–(10) and separating the coefficients at different orders of ε leads to

$$D_0^2 u_{n0} + 2u_{n0} - u_{(n-1)0} - u_{(n+1)0} + \bar{k} \Omega_0^2 D_0^2 (y_{n0} + u_{n0}) = 0$$
 (16)

$$\Omega_0^2 D_0^2 y_{n0} + y_{n0} - \alpha_1 y_{n0} = -\Omega_0^2 D_0^2 u_{n0}$$
 (17)

$$\alpha_2 D_0 v_{n0} + v_{n0} + \alpha_3 D_0 y_{n0} = 0 \tag{18}$$

order ε^1

$$D_0^2 u_{n1} + 2u_{n1} - u_{(n-1)1} - u_{(n+1)1} + \bar{k} \Omega_0^2 D_0^2 (y_{n1} + u_{n1})$$

$$= -2\bar{k} \Omega_0^2 D_0 D_1 (y_{n0} + u_{n0}) - 2D_0 D_1 u_{n0} - \alpha (u_{n0} - u_{(n-1)0})^3$$

$$- \alpha (u_{n0} - u_{(n+1)0})^3$$
(19)

$$\Omega_0^2 D_0^2 y_{n1} + y_{n1} - \alpha_1 v_{n1} = -\Omega_0^2 D_0^2 u_{n1} - 2\Omega_0^2 D_0 D_1 u_{n0}
- \alpha_r y_{n0}^3 - 2\Omega_0^2 D_0 D_1 y_{n0}$$
(20)

$$\alpha_2 D_0 v_{n1} + v_{n1} + \alpha_3 D_0 y_{n1} = -\alpha_2 D_1 v_{n0} - \alpha_3 D_1 y_{n0}$$
 (21)

Considering the linear problem (i.e., at order ε^0) and following Ref. [16], the solution of the system can be expressed using the Floquet–Bloch theory as

$$u_n = Ae^{i(nk - \omega T_0)} + \text{c.c}$$
 (22)

$$y_n = Be^{i(nk - \omega T_0)} + \text{c.c}$$
 (23)

$$v_n = Ce^{i(nk - \omega T_0)} + \text{c.c}$$
 (24)

where $i = \sqrt{-1}$, c.c is complex conjugate, and k = aq is the dimensionless wavenumber since q is the wavenumber. Following some algebraic manipulation [16], we obtain the dispersion relation as

$$-\omega^2 + (2 - 2\cos k) - \bar{k}\Omega_0^2\omega^2(1 + K_\omega) = 0$$
 (25)

where $K_{\omega} = \Omega_0^2 \omega^2 / (1 - \alpha_1 \Gamma - \Omega_0^2 \omega^2)$, and $\Gamma = i\alpha_3 \omega / (1 - i\alpha_2 \omega)$. Solving Eq. (25) reveals five roots. Four of them are complex

conjugate pairs, while the fifth is pure complex. Therefore, plotting the band structure of the propagating modes requires separating the four complex conjugate pairs only since the fifth root is always pure complex.

For the nonlinear problem (i.e., at order ε), one can write the nonlinear frequency equation, following Ref. [16], as

$$\omega_{nl} = \omega - \varepsilon \beta' \tag{26}$$

where β' is the phase resulting from expressing A in the polar form (i.e., where $A = \gamma e^{i\beta}$, where γ and β are real and represent the vibration amplitude and the phase, respectively) and is defined as

$$\beta' = c_1 \gamma_0^2 \tag{27}$$

The constant c_1 is defined as

$$c_1 = -\frac{gl + fh}{h^2 + g^2} \tag{28}$$

where g, l, h, and f are defined in Appendix for different sources of nonlinearity. It is noteworthy that the detailed derivations of the linear and nonlinear dispersion relations can be found in Ref. [16], while the analytical summarized results here are presented for completeness of the current work.

3 Analytical and Numerical Bandgaps

To check our analytical dispersion relations, we plot the analytical and numerical band structure of the system with electromechanical resonator in Fig. 2. To simulate the infinite periodic system, a very long chain consisting of 500 cells was used to construct the numerical band structure. Following Refs. [16,20,57], the parameters of the metamaterial with electromechanical resonator are chosen to be $\bar{k} = 1$, $\omega_n = \omega_d = 1000$, $k_1 = 10^6 \text{ N/M}$, $C_p = 13.3 \times$ 10^{-9} F, $R = 10^{7}\Omega$, and $\theta = 10^{-8}$ N/V. The mechanical parameters of the chain are chosen to demonstrate a locally resonant bandgap around $\omega = 1$, while the electromechanical parameters are chosen to represent the weak electromechanical coupling case. Numerical band structure can be obtained by exciting the system by a transient wave packet and integrating the system in Eqs. (8)–(10) numerically in MATLAB. This transient wave packet consists of $N_{\rm cy}$ periods confined within a slowly modulated Hann window. Therefore, the signal represents a minimal band of frequencies centered around the carrier frequency with quasi-monofrequency content. To limit the propagation in one direction, we define the initial conditions as

$$u_{m}(0) = \frac{1}{2} (H(m-1) - H(m-1 - N_{cy}2\pi/k))(1$$

$$-\cos(mk/N_{cy})) \sin(mk)$$

$$\dot{u}_{m}(0) = \frac{1}{2} (H(m-1) - H(m-1 - N_{cy}2\pi/k))$$

$$(-\omega_{n}\omega/N_{cy} \sin(mk/N_{cy}) \sin(mk)$$

$$-\omega_{n}\omega(1 - \cos(mk/N_{cy})) \cos(mk))$$
(30)

$$y_m(0) = K_{\omega} u_m(0)$$
 (31)

$$\dot{y}_m(0) = K_\omega \dot{u}_m(0) \tag{32}$$

$$v_m(0) = \Gamma K_\omega u_m(0) \tag{33}$$

where H(x) is the Heaviside function, and N_{cy} is the number of cycles and is chosen to be $N_{cy} = 7$ in this section.

Upon analyzing the output simulation results of the system excited by a specific wavenumber and its associated frequency using 2D fast Fourier transform (FFT), a point in the dispersion curves (frequency/wavenumber) can be determined by picking the peak of 2D FFT. Then, the complete band structure can be obtained from sweeping the wavenumber over the first Brillouin zone at the acoustic and optical modes.

Before presenting the analytical and numerical results, it is worthy to define the different wavelength limits. Note that the wavelength and wavenumber are inversely proportional to each other. Therefore, the long-wavelength limit is defined at relatively small value of wavenumber (i.e., $k \sim \pi/9$ in Sec.4) within the first irreducible Brillouin zone (i.e., $k \in [0, \pi]$). On the other hand, the short-wavelength limit is associated with relatively large value of wavenumber (i.e., $k \sim 7\pi/9$ in Sec. 4). At a relatively moderate value of wavenumber, we define the medium-wavelength limit (i.e., $k \sim \pi/2$ in Sec. 4).

Figure 2(a) depicts the linear and nonlinear analytical band structures (solid lines) and the nonlinear numerical band structure (asterisks) for the nonlinear chain case (i.e., the nonlinearity in the local resonator is set to zero). The analytical results (solid lines) demonstrate that hardening nonlinearity shifts the dispersion curves up as compared to the linear curves. This shift is more pronounced at the long-wavelength limit (i.e., large values of k). Moreover, the numerical integration results (asterisks) also demonstrate that the analytical solution can predict the boundary of the band structure (i.e., cutoff and cut-on frequencies of the optical and acoustics modes), but fail to capture the significant frequency shift, which is observed numerically at the medium-wavelength limit (i.e., at values around $k = \pi/2$) in the optical mode. In particular, if the system is excited by input waves with frequencies within the medium-wavelength limits (region inside the box in Fig. 2(a)), the output waves appear at different frequency/wavenumber limits (region inside the circles on long and short-wavelength limits in Fig. 2(a)), coinciding with the linear dispersion curves. Since the input frequency is altered by the nonlinear metamaterial, a frequency shift is anticipated in this region. The observed frequency shift may be attributed to second harmonic generation due to nonlineairty in the chain [58]. Moreover, it should be noted that this frequency shift can only be observed in the case of transient wave inputs but not for harmonic wave inputs [20]. This region of frequency shift is referred as pseudo gap in the literature. This frequency shift will be used to design our electromechanical resonator and will be discussed further using the spectro-spatial analyses in the next section.

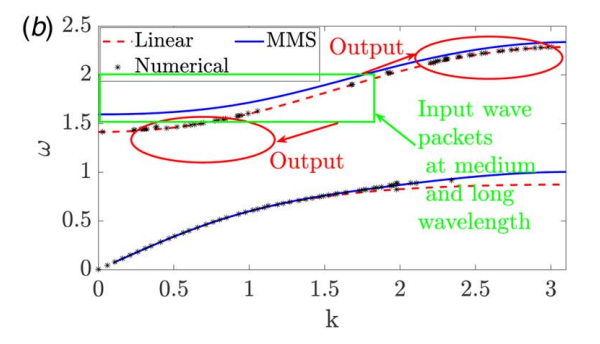


Fig. 2 Band structure for linear and nonlinear metamaterials with electromechanical resonators obtained analytically and numerically: (a) nonlinear chain case $\varepsilon A^2 \alpha = 0.06$, $\varepsilon A^2 \alpha_r = 0$ and (b) nonlinear resonator case $\varepsilon A^2 \alpha = 0$, $\varepsilon A^2 \alpha_r = 0.06$

After discussing the effect of nonlinearity that stems from the nonlinear chain, we present the band structure for the nonlinear electromechanical resonator in Fig. 2(b). Unlike the case of nonlinearity in the chain, the analytical results demonstrate that hardening nonlinearity shifts the dispersion curves up not only in the medium-/ short-wavelength limits but also at the long-wavelength limit. This shift is more significant at frequencies near the fundamental frequency of the electromechanical resonator. Therefore, the effect of nonlinearity at the long-wavelength limit in the optical mode can be realized, unlike the case of nonlinear chain where the effect of nonlinearity is limited to the medium-/short-wavelength limits. For the case of resonator nonlinearity, numerical results (asterisks) indicate that input waves with frequencies within the medium and long-wavelength limits (regions inside the box in Fig. 2(a)) in the optical mode appear at different regions as an output wave. These regions are highlighted inside the circles and coincide with the linear dispersion curves. This suggests that the analytical solution fails to predict the band structure in these regions due to the significant frequency shift. The observed frequency shift may be attributed to second harmonic generation due to nonlinearity in the local resonator [58]. This shift will be further investigated in the next section. Similar frequency shift appears at the short-wavelength limit in the acoustics mode, where the effect of the electromechanical resonator's nonlinearity is maximum in this mode due to close tuning between the electromechanical resonator and frequencies in this region.

In regions where our solution fails, higher-order perturbations [59] and wavenumber-space band clipping [60] may need to be considered to capture the frequency/wavenumber shift in these regions accurately. The results of band structures in Fig. 2 indicate the possibility of a significant frequency shift; however, they do not reveal any further details on the nature of the wave distortion, the output frequency content, and the spatial properties. Therefore, in the next section, we employ different signal processing techniques to investigate the spectro-spatial features and obtain further detailed information.

4 Spectro-Spatial Analysis

To further demonstrate the significant frequency shift at the medium-/long-wavelength limits in the optical mode for both types (i.e., hardening and softening) and sources (i.e., chain and resonator) of nonlinearities, we analyze the numerical results further by utilizing different signal processing techniques.

We plot the spatial profile of the input and output voltage signals harvested by the electromechanical resonator at a snapshot during the time of the simulation in Fig. 3. To avoid the appearance of any reflective waves, the snapshot is presented before the wave arrives at the other end of the chain. Since we are simulating a very long chain (i.e., 500 cells), we anticipated that the qualitative behavior at the output cell would be similar to the snapshot that we presented. Therefore, we refer to the snapshot as the output wave in the following discussion. At long-wavelength limit (i.e., $k \sim \pi/9$) with chain nonlinearity (Fig. 3(a)), the results indicate that the chain nonlinearity has no effect on the output wave. In particular, the output wave is not distorted at all at this wavelength limit for chain nonlinearity. On the other hand, results at mediumwavelength limit (i.e., $k \sim \pi/2$) demonstrate that the input signal is severely distorted and broken into several components, as shown in Fig. 3(b). These components are (1) one localized high-amplitude wave (solitary wave) and (2) two stretched and low-amplitude waves (dispersive waves). This indicates that the output wave appears at different frequencies other than the input frequency.

For nonlinear electromechanical resonator case, the results demonstrate that severe output wave distortion can be observed at long-wavelength limit (i.e., $k \sim \pi/9$; Fig. 3(c)) and medium-wavelength limit (i.e., $k \sim \pi/2$; Fig. 3(d)). Unlike the case of chain nonlinearity, severe wave distortion at long-wavelength limit (i.e., $k \sim \pi/9$) due to resonator nonlinearity can be observed. Therefore, the input signal at this wavelength limit can appear at frequencies other than the input frequency. In addition, the wave distortion at medium wavelength limit (i.e., $k \sim \pi/2$) due to resonator nonlinearity is similar to the distortion observed in the nonlinear chain case at the same wavelength limit. Although the wave distortion in the case of nonlinear resonator is less severe than the distortion in the case of nonlinear chain, the case of nonlinear resonator can offer a significant frequency shift at the long-wavelength limit (i.e., $k \sim \pi/9$) unlike the case of nonlinear chain.

The energy content of the frequency/wavenumber components is shown in Fig. 4. The figure presents the short-term Fourier transform (STFT) of the input/output signals' spatial components over the spatial domain. We use a Hann window with the size of the input signal to contain the propagating wave. For nonlinear chain case, the results indicate that the output voltage signal is broken into three components for hardening nonlinearity (Fig. 4(a)) and into two components for softening nonlinearity (Fig. 4(b)). For hardening nonlinearity, the first component appears at wavenumber/frequency above the input wavenumber/frequency window

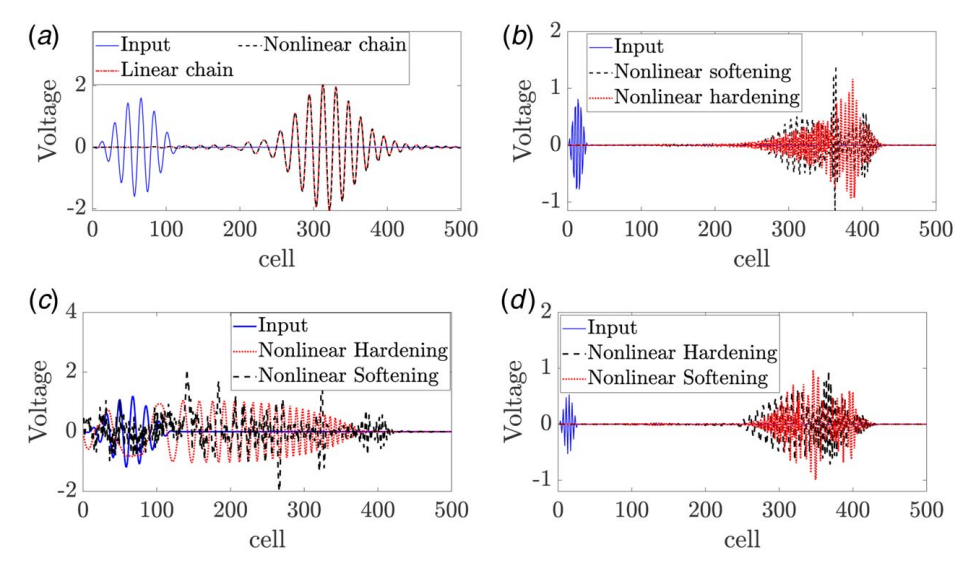


Fig. 3 Spatial profile of the input/output voltage in the optical mode: (a) $k = \pi/9$, $|\varepsilon A^2 \alpha| = 0.03$, $|\varepsilon A^2 \alpha_r| = 0$, (b) $k = \pi/2$, $|\varepsilon A^2 \alpha| = 0.03$, $|\varepsilon A^2 \alpha_r| = 0$, (c) $k = \pi/9$, $|\varepsilon A^2 \alpha| = 0$, $|\varepsilon A^2 \alpha_r| = 0.03$, and (d) $k = \pi/2$, $|\varepsilon A^2 \alpha| = 0$, $|\varepsilon A^2 \alpha_r| = 0.03$

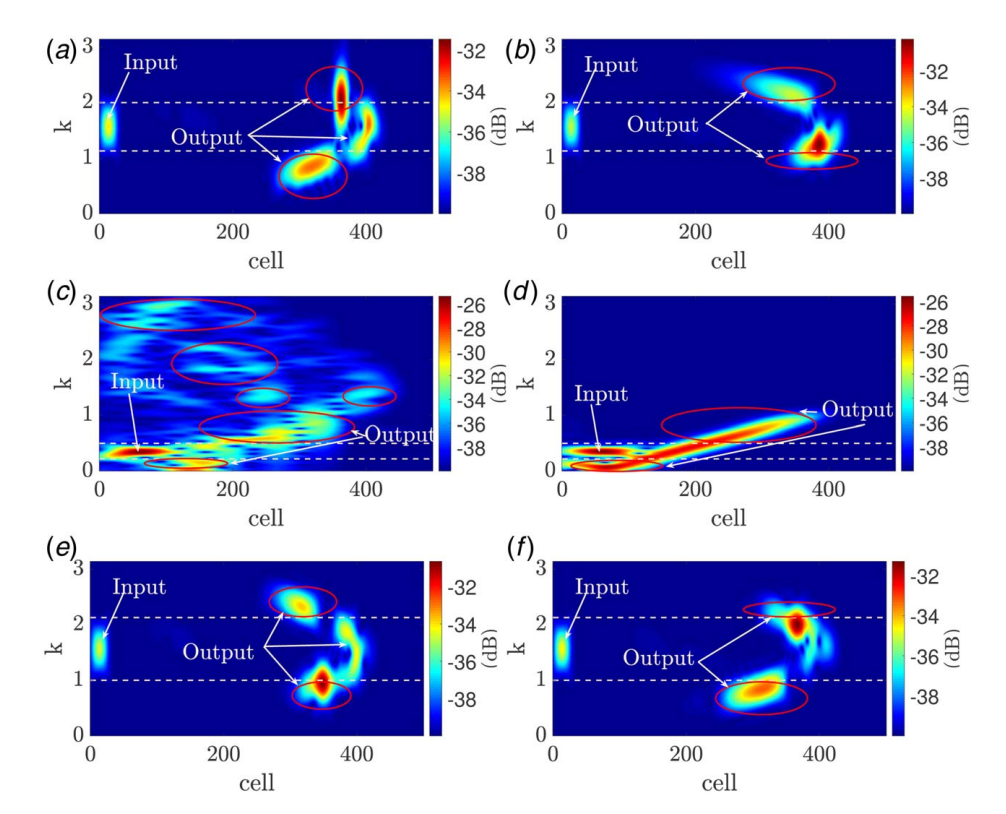


Fig. 4 Spectrograms of the input/output voltage in the optical mode: (a) $k = \pi/2$, $\varepsilon^2 A \alpha = 0.03$, $\varepsilon^2 A \alpha_r = 0$, (b) $k = \pi/2$, $\varepsilon^2 A \alpha = -0.03$, $\varepsilon^2 A \alpha_r = 0$, (c) $k = \pi/9$, $\varepsilon^2 A \alpha = 0$, $\varepsilon^2 A \alpha_r = -0.03$, (d) $k = \pi/9$, $\varepsilon^2 A \alpha = 0$, $\varepsilon^2 A \alpha_r = 0.03$, (e) $k = \pi/2$, $\varepsilon^2 A \alpha = 0$, $\varepsilon^2 A \alpha_r = -0.03$, and (f) $k = \pi/2$, $\varepsilon^2 A \alpha = 0$, $\varepsilon^2 A \alpha_r = 0.03$

and it has the highest energy content. This is not surprising since the band structure figures showed that hardening nonlinearity shifts the dispersion curves up; therefore, the highest energy content component appears above the input frequency/wavenumber window. The second component appears inside the initial window and it has the lowest energy content. Finally, the third component is shifted below the initial window and its energy content is between the first and second components. Thus, most of the energy content of the input signal (i.e., inside the ellipses on the figure) appears at output signal frequencies different than the input signal frequencies. This shows a good potential for using the proposed system to design an electromechanical diode. For softening nonlinearity, the first component appears outside the input frequency/wavenumber window and it has low energy content. The second component appears below the input window range and has the highest energy content. Although the case of softening nonlinearity shows also a significant frequency shift (i.e., inside the ellipses on the figure), a significant portion of the energy content appears inside the input frequency/wavenumber window unlike the case of hardening nonlinearity. Therefore, we anticipate that hardening chain has better performance than softening chain in terms of non-reciprocal energy transmission.

For the case of nonlinear resonator, the results demonstrate a significant frequency shift at the long-wavelength limit (i.e., $k \sim \pi/9$) unlike the case of nonlinear chain. For softening nonlinearity (Fig. 4(c)), the STFT of the output voltage wave shows the presence of multiple frequency/wavenumber components. These components stretch over a wide range of frequency/wavenumber. Most of those components appear outside the input frequency/wavenumber window (i.e., components confined inside the ellipses). For hardening nonlinearity (Fig. 4(d)), the energy content also extends outside the input frequency/wavenumber window. In particular, one of the output component stretches inside and outside the input window, while the other component is completely outside the input window. Therefore, hardening nonlinearity can also result in significant frequency shift at long-wavelength limit (i.e., $k \sim \pi/9$) due to

resonator nonlinearity. However, the frequency/wavenumber range at which the output signal stretches is narrower than that for the softening nonlinearity case. At medium-wavelength limit (i.e., $k \sim \pi/2$), the output signal is also broken into multiple components due to resonator nonlinearity similar to the case of nonlinear chain. For instance, softening nonlinearity breaks the output signal into three components as shown in Fig. 4(e). The highest energy content component appears below the input frequency/wavenumber window, while the lowest energy content component appears inside the input window. The third component has a moderate energy content and lies outside the input window. Since most of the output energy content appears outside the input window (i.e., components confined inside the ellipses), the resonator nonlinearity can also significantly shift the frequency content of the input signal at medium-wavelength limit (i.e., $k \sim \pi/2$). Therefore, this type of nonlinearity is suitable to design an electromechanical diode at medium- and long-wavelength limits. For hardening nonlinearity case (Fig. 4(e)), resonator nonlinearity splits the output signal into two components. The first one has high energy content and is shifted up due to hardening nonlinearity, while the second has low energy content and appears below the input window. Since some of the energy content also appears outside the input window (highlighted by ellipses in the figure), hardening nonlinearity can also show a significant frequency shift. However, this shift is not as significant as the shift in the case of softening nonlinearity for the resonator nonlinearity case.

Further demonstration of the significant frequency shift in the system can be obtained by plotting the contour of 2D FFT for the output signal as shown in Fig. 5. The results also indicate that the output signal frequency components are distributed over a wide range of frequencies, indicating the presence of significant frequency conversion. For instance, chains with hardening nonlinearity (Fig. 5(a)) distribute the energy content over a wider range of frequencies as compared to the case of softening nonlinearity (Fig. 5(b)). Moreover, the high energy components are distributed over wavenumbers above and below the medium-wavelength

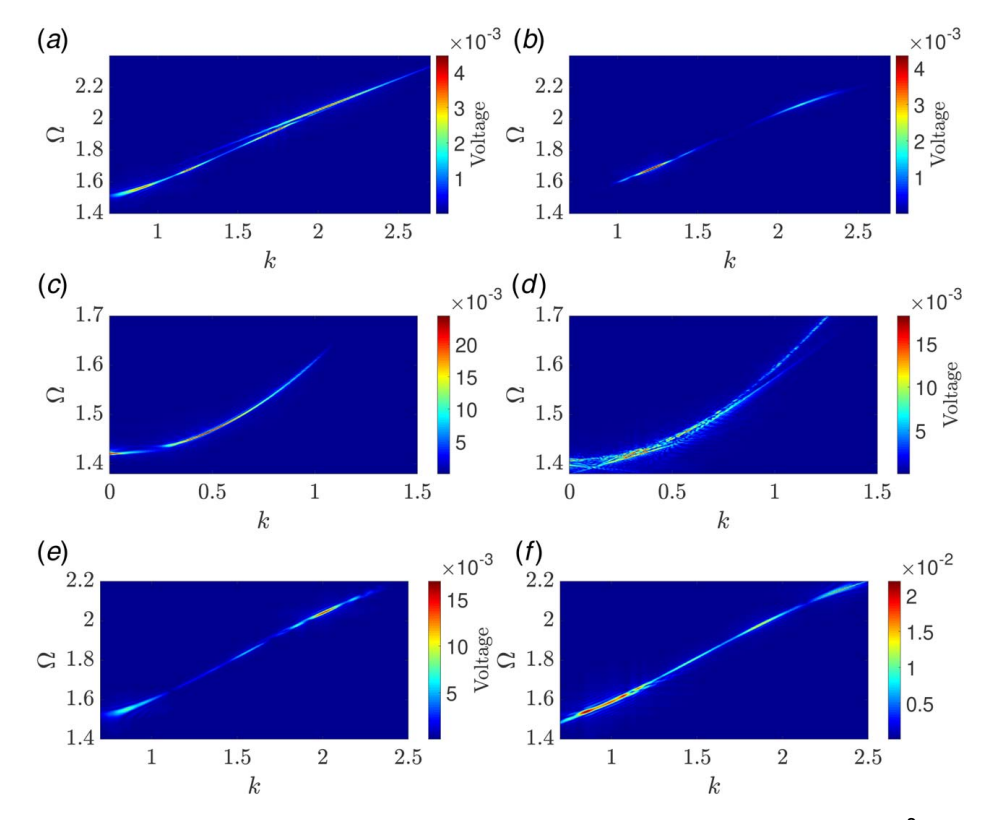


Fig. 5 Images of the 2D FFT contour of the output voltage in the optical mode: (a) $k = \pi/2$, $\varepsilon^2 A \alpha = 0.03$, $\varepsilon^2 A \alpha_r = 0$, (b) $k = \pi/2$, $\varepsilon^2 A \alpha = -0.03$, $\varepsilon^2 A \alpha_r = 0$, (c) $k = \pi/9$, $\varepsilon^2 A \alpha = 0$, $\varepsilon^2 A \alpha_r = 0.03$, (d) $k = \pi/9$, $\varepsilon^2 A \alpha = 0$, $\varepsilon^2 A \alpha_r = -0.03$, (e) $k = \pi/2$, $\varepsilon^2 A \alpha = 0$, $\varepsilon^2 A \alpha_r = 0.03$, and (f) $k = \pi/2$, $\varepsilon^2 A \alpha = 0$, $\varepsilon^2 A \alpha_r = -0.03$

limit (i.e., wavelength of the input signal $(k \sim \pi/2)$). In particular, most of the energy content is concentrated above the input signal frequency for hardening chains, while it is concentrated below the input signal frequency for softening chain. On the other hand, the results for resonator nonlinearity (Figs. 5(c)–5(f)) indicate similar significant frequency conversion at both long- and mediumwavelength limits unlike the case of chain nonlinearity, which limits the frequency conversion to the medium-wavelength limit (i.e., $k \sim \pi/2$). For instance, hardening nonlinearity stretches the frequency content over a wide range of frequencies, as shown in Fig. 5(c). This stretch is even wider for the case of softening resonator frequency, as depicted in Fig. 5(d). Beyond the significant frequency conversion obtained at long-wavelength limit (i.e., $k \sim \pi/9$), resonator nonlinearity can also show a significant frequency shift at medium-wavelength limit (i.e., $k \sim \pi/2$). This shift is demonstrated by the clear stretching of the signal over wider range of frequencies for the hardening nonlinearity in Fig. 5(e) and softening nonlinearity in Fig. 5(f).

The discussion in this section emphasizes the presence of significant frequency shift (conversion) due to the nonlinearity in the proposed structure. This frequency conversion can be observed at medium-wavelength limit (i.e., $k \sim \pi/2$) for both types of nonlinearity and at long-wavelength limit (i.e., $k \sim \pi/9$) in the case of nonlinear resonator only. In the following section, we will then investigate how to design an electromechanical diode based on the observed direction. Moreover, we will also investigate the anticipated increase in the frequency band of the diode by the resonator nonlinearity since it shows a significant frequency shift at both long- and medium-wavelength limits.

5 Electromechanical Diode

Based on the significant frequency shift observed in the previous sections, we design an electromechanical diode for direction-biased waveguide applications. This diode allows waves to propagate in

one direction, therefore harvesting energy and sensing waves propagating in only one direction. A schematic diagram for the proposed electromechanical diode is shown in Fig. 6. The electromechanical diode is constructed from linear and nonlinear metamaterials. The nonlinear metamaterial with parameters defined above has a significant frequency shift region at medium-wavelength limit (i.e., $k \sim \pi/2$) in the optical mode for the case of nonlinear chain, and long-/medium-wavelength limit for the case of the nonlinear resonator in the optical mode. The linear metamaterial is designed to have a bandgap tuned to the medium (i.e., $k \sim \pi/2$) or longwavelength (i.e., $k \sim \pi/9$) limits in the optical mode. Any wave with frequency in these regions and propagating in the nonlinear metamaterial has some energy content with frequencies different than the excitation frequency and outside these regions due to the significant frequency conversion. The output signal can propagate into the attached linear metamaterial since its bandgap is tuned to the input frequency. Therefore, voltage can be harvested in the forward configuration. On the other hand, a wave with the same frequency band does not propagate when it excites the linear metamaterial in the backward configuration. Therefore, voltage cannot be harvested in this configuration.

The combination of the linear and nonlinear chains constructing the electromechanical diode for forward and backward configurations is shown in Fig. 7. The nonlinear metamaterial consists of 350 cells with the same parameters defined in the previous sections and the nonlinearity stems from the chain or electromechanical resonator. The linear metamaterial consists of 150 cells. The parameters of the linear metamaterial are chosen to tune the chain bandgap to the significant frequency shift region in the nonlinear metamaterial. It is noteworthy here that we chose the mass of the linear chain to be equal to the nonlinear chain mass to reduce the impedance mismatch. The linear chain has a stiffness, K_l , mass, M_l , local resonator stiffness, k_{1l} , and local resonator mass, m_{pl} . We assume that the linear chain has electromechanical coupling terms similar to those in the

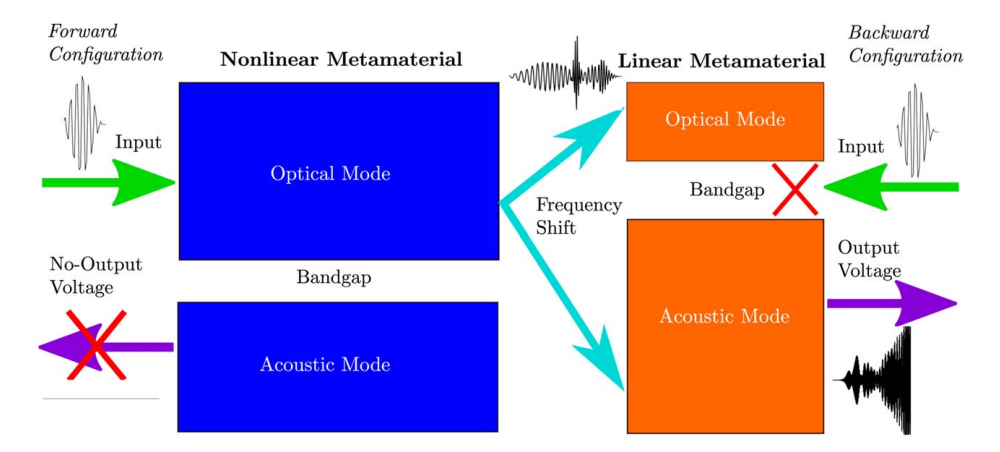
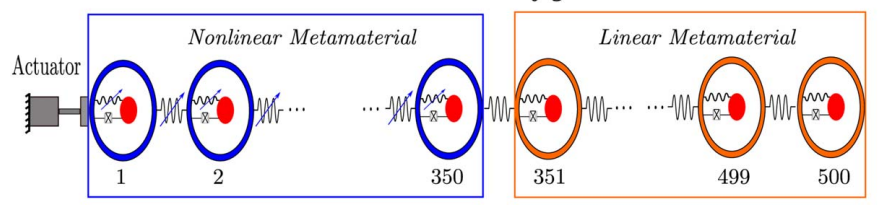


Fig. 6 A schematic diagram for the electromechanical diode

Forward Configuration



Backward Configuration

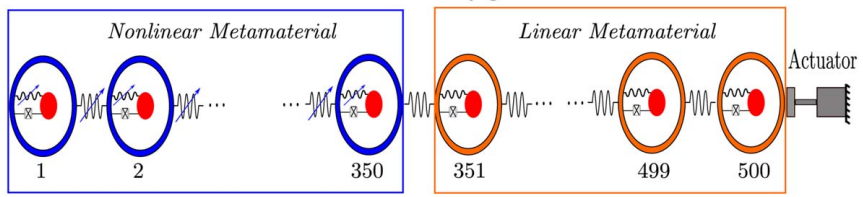


Fig. 7 A schematic diagram for the forward and backward configurations

nonlinear chain. We define the following set of dimensionless parameters for the linear chain

$$\bar{k}_l = K_l/K; \, \bar{M}_l = M_l/M; \, \bar{k}_p = k_{1l}/k1; \, \bar{m}_p = m_{pl}/m_p$$
 (34)

where \bar{m}_p is set to 1 for all cases to reduce the impedance mismatch, and $N_{cv} = 60$ for all input signals.

For a narrow band frequency excitation, we excite both configurations by N_{cv} period of burst signal defined as

$$F_{ex} = \frac{1}{2} A \left[H(t) - H \left(t - \frac{2\pi\omega_n N_{cy}}{\omega\omega_d} \right) \right]$$

$$\times \left[\frac{1}{2} 1 - \cos \left(\frac{\omega_d \omega}{\omega_n N_{cy}} t \right) \right] \sin \left(\frac{\omega_d \omega}{\omega_n} t \right)$$
(35)

where N_{cy} = 60. It is noteworthy that the frequency distribution of this signal becomes narrower with increasing the number of periods (waves) in the input force.

To evaluate the performance of the electromechanical diode, we need to calculate the input and output energy harvested in the 1st and 500th cells. The power can be determined as

$$P_n = \frac{V_n^2}{R} \tag{36}$$

In each configuration, the transmission ratio can be determined as

$$Tr_f = \frac{\int_0^{\tau} P_{500} d\tau}{\int_0^{\tau} P_1 d\tau}$$
 (37)

$$Tr_b = \frac{\int_0^{\tau} P_1 d\tau}{\int_0^{\tau} P_{500} d\tau} \tag{38}$$

where Tr_f and Tr_b are the transmission ratios for the forward and backward configurations, respectively. Upon calculating the transmission ratios for each configuration, the asymmetric ratio can be calculated as

$$\sigma = \frac{Tr_f}{Tr_b} \tag{39}$$

Before analyzing the proposed diode response, we show the transient input force profile in Fig. 8. The input force was generated using Eq. (35). This force will be applied in all backward and forward configurations. For excitation within the long-wavelength limit (i.e., $k = \pi/9$), the input force is shown in Fig. 8 for $\omega = 1.5$. On the other hand, Fig. 8(b) presents the input force with $\omega = 2$ for excitation within the medium-wavelength limit (i.e., $k = \pi/2$). It is noteworthy that the harvested voltage in the input cell, which is shown in Figs. 9–11, can differ from the input force profile, especially, in the case of nonlinear resonator. Indeed, the nonlinearity in the local resonator may affect the nonlinear local resonator response resulting in a wave distortion.

For the case of nonlinear chain, the response of the forward and backward configurations for different types of nonlinearity is shown in Fig. 9. At medium-wavelength limit (i.e., $k \sim \pi/2$), we excite the system by a signal with $\omega = 2$, tuning the bandgap of the linear chain to the medium-wavelength limit (i.e., $k \sim \pi/2$) in the optical mode in the nonlinear chain. For hardening chain, the

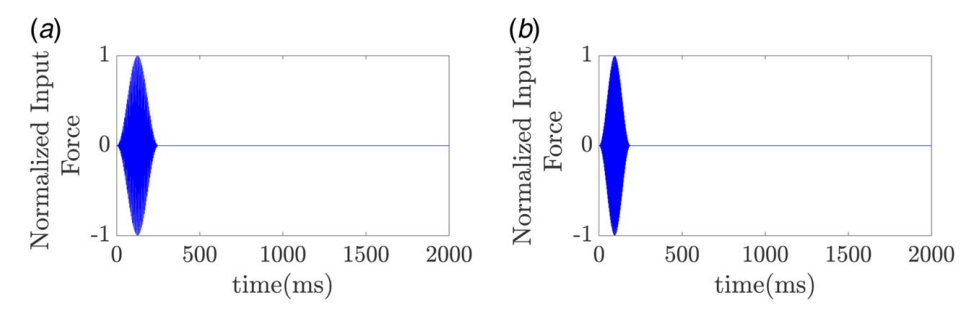


Fig. 8 Normalized input force applied to the structure in both configurations: (a) $\omega = 1.5$ and (b) $\omega = 2$

results indicate that the wave can propagate in the forward configuration (Fig. 9(a)); therefore, voltage can be sensed on the other end. However, the input wave cannot propagate in the backward configuration, thus no voltage can be harvested and the system acts as direction-biased waveguide, as shown in Fig. 9(b). For forward configuration, the transmission ratio is $Tr_f = 0.99$. The achieved transmission ratio in the forward configuration is high as compared to Refs. [15,52]. The transmission ratio for the backward configuration is $Tr_b \approx 10^{-7}$. Moreover, the asymmetric ratio for the electromechanical diode is $\sigma \approx 6.4 \times 10^6$. These results show that the proposed electromechanical diode has a higher asymmetric ratio with higher transmission ratios than mechanical diodes reported in the literature. For instance, the asymmetric ratio in Refs. [15,52] is $\sigma \approx 10^4$ and both reported low transmission ratios. For softening chain, the wave can also propagate in the forward configuration and voltage can be

harvested on the other end, as shown in Fig. 9(c). Moreover, waves cannot propagate in the backward configuration for softening nonlinearity as shown in Fig. 9(d). This indicates that softening nonlinearity can also be used in designing electromechanical diodes. However, the harvested voltage on the other end is lower in this case as compared to the hardening chain case in Fig. 9(a). In particular, the transmission ratio for the forward configuration is $Tr_f = 0.2457$, while the asymmetric ratio for the electromechanical diode is $\sigma \approx 1.9 \times 10^6$. Increasing the strength of nonlinearity in the chain can increase the transmission ratio for the forward configuration. For instance, increasing hardening nonlinearity in the chain can significantly increase the output voltage with transmission ratio $Tr_f \approx 1.3582$ and asymmetric ratio $\sigma \approx 8.8 \times 10^6$, as shown in Fig. 9(e). It is noteworthy that the transmission ratio for the voltage can exceed 1 as the voltage wave can be amplified at some particular

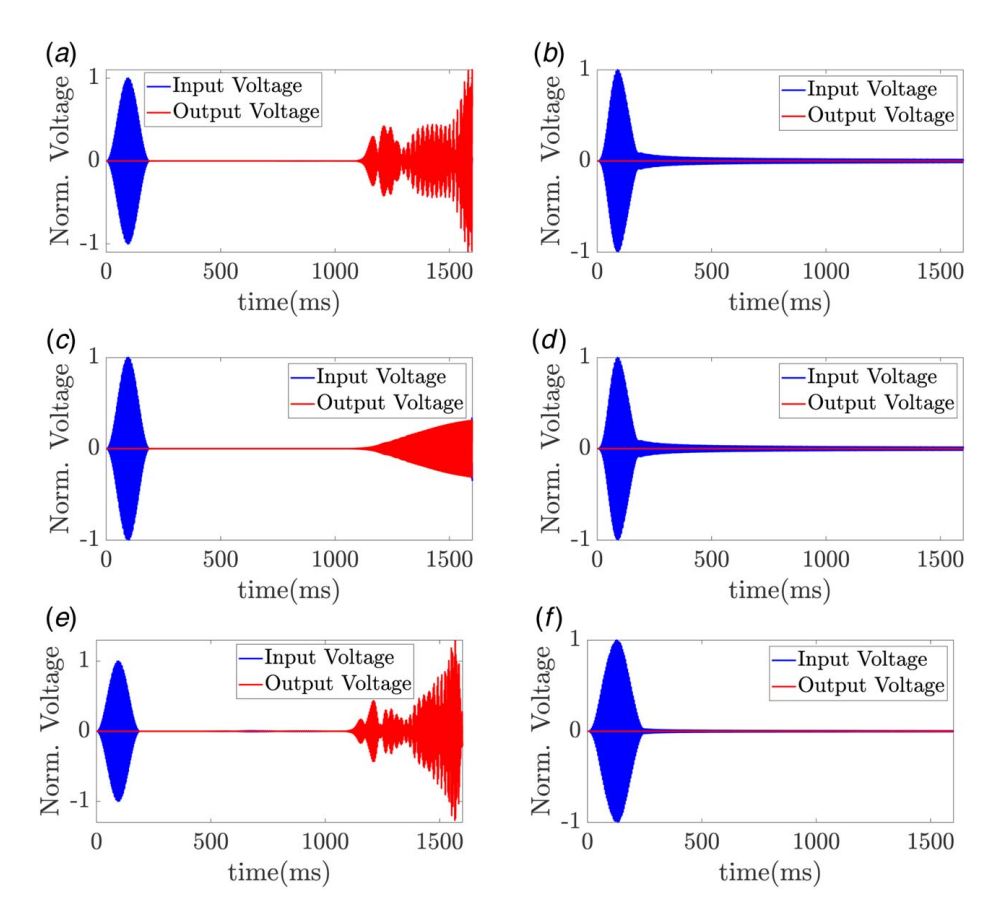


Fig. 9 Time response of electromechanical diode in forward and backward configurations for the case of nonlinear chain: (a) forward configuration, $\omega=2$, $\bar{k}_l=1.3$, $\bar{k}_p=0.16$, $\bar{m}_p=0.04$, $\varepsilon^2 A \alpha=0.03$, $\varepsilon^2 A \alpha_r=0$, (b) backward configuration of (a), (c) forward configuration, $\omega=2$, $\bar{k}_l=1.3$, $\bar{k}_p=0.16$, $\bar{m}_p=0.04$, $\varepsilon^2 A \alpha=0.03$, $\varepsilon^2 A \alpha_r=0$, (d) backward configuration of (c), (e) forward configuration, $\omega=2$, $\bar{k}_l=1.3$, $\bar{k}_p=0.16$, $\bar{m}_p=0.04$, $\varepsilon^2 A \alpha=0.06$, $\varepsilon^2 A \alpha_r=0$, and (f) forward configuration, $\omega=1.5$, $\bar{k}_l=0.78$, $\bar{k}_p=0.21$, $\bar{m}_p=0.09$, $\varepsilon^2 A \alpha=0.03$, $\varepsilon^2 A \alpha_r=0$

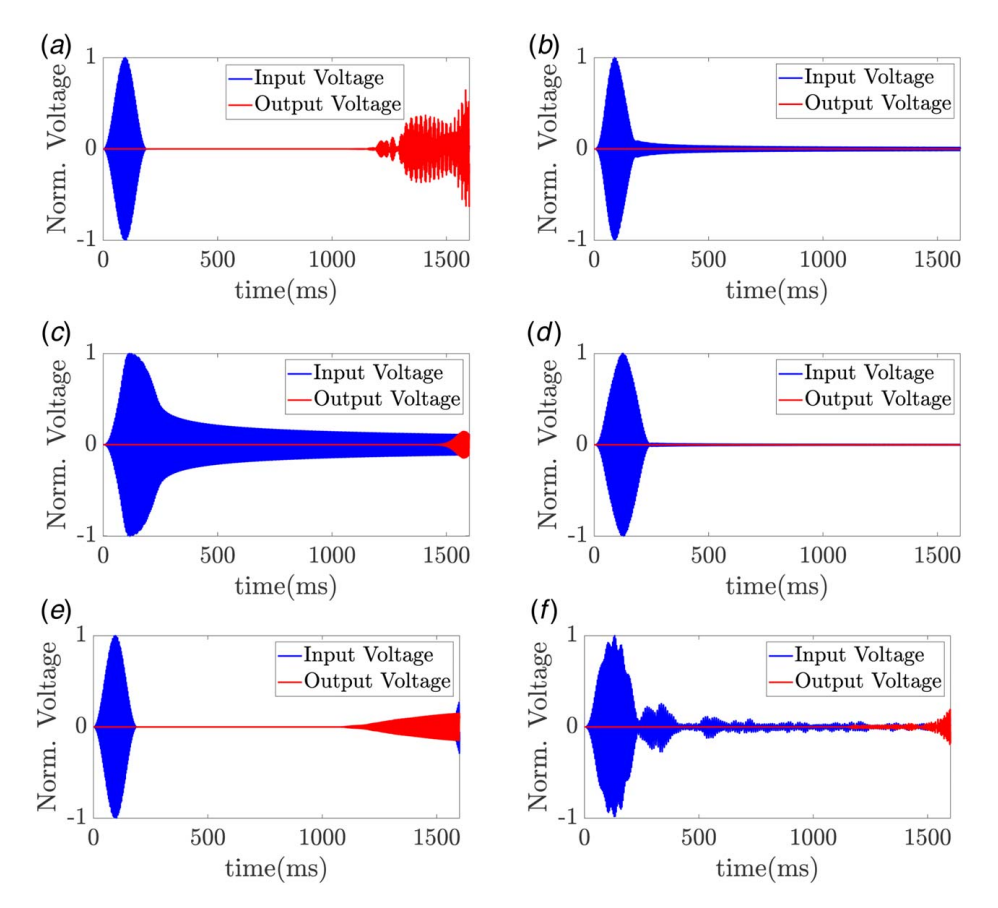


Fig. 10 Time response of electromechanical diode in forward and backward configurations for the case of nonlinear resonator: (a) forward configuration, $\omega=2$, $\bar{k}_l=1.3$, $\bar{k}_p=0.16$, $\bar{m}_p=0.04$, $\varepsilon^2 A \alpha=0$, $\varepsilon^2 A \alpha_r=0.03$, (b) backward configuration of (a), (c) forward configuration, $\omega=1.5$, $\bar{k}_l=0.78$, $\bar{k}_p=0.21$, $\bar{m}_p=0.09$, $\varepsilon^2 A \alpha=0$, $\varepsilon^2 A \alpha_r=0.03$, (d) backward configuration of (c), (e) forward configuration, $\omega=2$, $\bar{k}_l=1.3$, $\bar{k}_p=0.16$, $\bar{m}_p=0.04$, $\varepsilon^2 A \alpha=0$, $\varepsilon^2 A \alpha_r=-0.03$, and (f) forward configuration, $\omega=1.5$, $\bar{k}_l=0.78$, $\bar{k}_p=0.21$, $\bar{m}_p=0.09$, $\varepsilon^2 A \alpha=0$, $\varepsilon^2 A \alpha_r=-0.03$

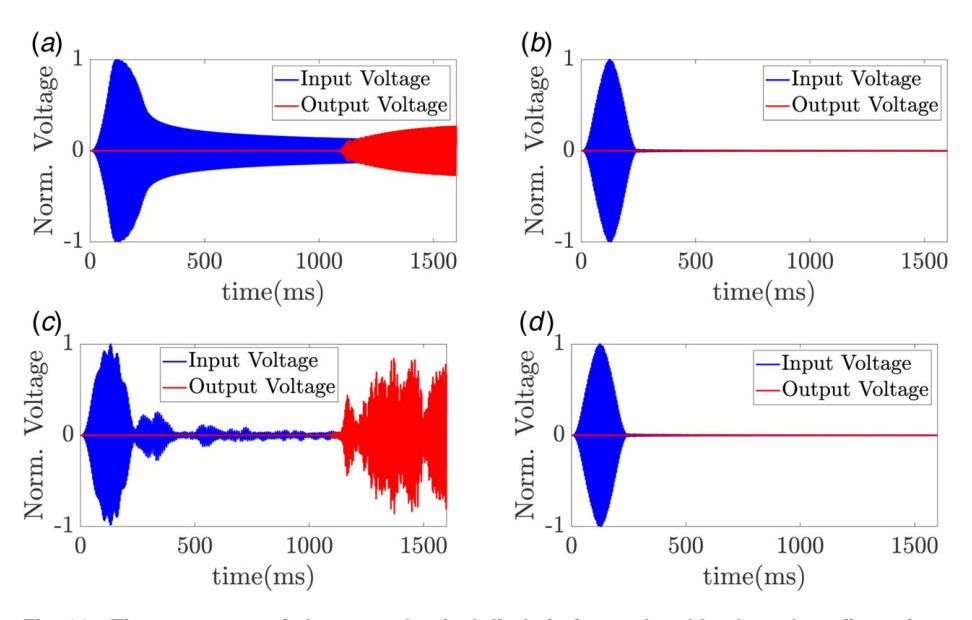


Fig. 11 Time response of electromechanical diode in forward and backward configurations for the case of nonlinear resonator: (a) forward configuration, $\omega=1.5$, $\bar{k}_{I}=1.5$, $\bar{k}_{P}=0.37$, $\bar{m}_{p}=0.17$, $\varepsilon^{2}A\alpha=0$, $\varepsilon^{2}A\alpha_{r}=0.03$, (b) backward configuration, $\omega=1.5$, $\bar{k}_{I}=1.5$, $\bar{k}_{P}=0.37$, $\bar{m}_{p}=0.17$, $\varepsilon^{2}A\alpha=0$, $\varepsilon^{2}A\alpha_{r}=0.03$, (c) forward configuration, $\omega=1.5$, $\bar{k}_{I}=1.5$, $\bar{k}_{P}=0.37$, $\bar{m}_{p}=0.17$, $\varepsilon^{2}A\alpha=0$, $\varepsilon^{2}A\alpha_{r}=-0.03$, and (d) backward configuration, $\omega=1.5$, $\bar{k}_{I}=1.5$, $\bar{k}_{P}=0.37$, $\bar{m}_{P}=0.37$, $\bar{m}_{P}=0.17$, $\varepsilon^{2}A\alpha=0$, $\varepsilon^{2}A\alpha_{r}=-0.03$

frequencies [16]. Finally, we excite our system with nonlinear chain at frequency within the long-wavelength limit (i.e., $\omega=1.5$) with linear chain's bandgap tuned to this limit. The response of the forward configuration is shown in Fig. 9(f). The result indicates that the wave does not propagate within the long-wavelength limit (i.e., $k \sim \pi/9$); therefore, voltage cannot be harvested at the other end. This is not surprising since we showed earlier that the nonlinearity has no effect on the wave propagation at the long-wavelength limit (i.e., $k \sim \pi/9$) in the case of nonlinear chain.

For the case of nonlinear resonator, the response of the forward and backward configurations for different types of nonlinearity is shown in Fig. 10. At medium-wavelength limit (i.e., $k \sim \pi/2$), we excite the system by a signal within the medium-wavelength limit (i.e., $k \sim \pi/2$) in the optical mode (i.e., $\omega = 2$) by tuning the bandgap of the linear chain to this region. For hardening nonlinearity, the results indicate that the nonlinear resonator case can also show non-reciprocity in wave propagation. For instance, the wave can propagate in the forward propagation (Fig. 10(a)) and get blocked in the backward configuration (Fig. 10(b)). However, output voltage in this case is lower compared to the case of nonlinear chain. For this particular case, the transmission ratio for the forward configuration is $Tr_f \approx 0.3467$ and asymmetric ratio $\sigma \approx 1.9$ $\times 10^6$. At long-wavelength limit (i.e., $\omega = 1.5$ and the linear bandgap is tuned to this limit), unlike the case of nonlinear chain, the wave can propagate in the forward configuration (Fig. 10(c)), but it cannot propagate in the backward configuration (Fig. 10(d)). The transmission ratio for this case is $Tr_f \approx 4 \times 10^{-3}$, and the asymmetric ratio is $\sigma \approx 2.2 \times 10^5$. Although the performance of the electromechanical diode in the case of nonlinear resonator at medium-wavelength limit (i.e., $k \sim \pi/2$) is weaker than the case of nonlinear chain due to lower transmission and asymmetric ratios, the electromechanical diode can be operated at the long-wavelength limit (i.e., $k \sim \pi/9$) in the case of nonlinear resonator unlike the case of nonlinear chain where no voltage can be sensed at the other end. This is not surprising since the spectro-spatial analysis showed the presence of significant frequency shift at the long-wavelength limit (i.e., $k \sim \pi/9$) for the nonlinear resonator case. It is noteworthy that the harvested voltage in the input cell is severely distorted at the long-wavelength limit (i.e., $k \sim \pi/9$). Since this voltage represents the harvested voltage in the nonlinear local resonator, the wave is significantly distorted as it interacts with the nonlinear local resonator. Note that this outcome is the effect of strong nonlinearity in this region. However, the input mechanical wave packet should be the same for all cases, as shown in Fig. 8. The nonlinearity in the local resonator also results in long duration oscillations to produce output voltage, as depicted in Fig. 10(c). Yet, the system still demonstrates non-reciprocity in its response. For softening nonlinearity, an electromechanical diode can also be operated at medium-/long-wavelength limits in the case of nonlinear resonator. For instance, Fig. 10(e) shows that voltage can be sensed at the other end at medium-wavelength limit (i.e., $k \sim \pi/2$) with transmission ratio $Tr_f \approx 0.059$ and asymmetric ratio $\sigma \approx 3.85 \times 10^5$. On the other hand, Fig. 10(f) shows that voltage can be sensed at the other end at long-wavelength limit (i.e., $k \sim \pi/9$) with transmission ratio $Tr_f \approx 4.3 \times 10^{-3}$ and asymmetric ratio $\sigma \approx 2.4 \times 10^5$. The results of softening nonlinearity indicate that an electromechanical diode with softening nonlinearity outperforms diodes with hardening nonlinearity at long-wavelength limit (i.e., $k \sim \pi/9$). However, the presence of hardening nonlinearity in the resonator shows better performance at medium-wavelength limit (i.e., $k \sim \pi/2$).

In order to obtain a linear chain's bandgap tuned to the long-wavelength limit (e.g., the frequencies of the bandgap for linear chain ranges between 1.41 and 1.6), many options can be explored within a small margin of frequency change (± 0.01). We search for linear chain's bandgap limits within $\bar{k}_l = 0.5 - 1.5$, $\bar{k}_p = 0.01 - 1$, and $\bar{m}_p = 0.01 - 1$. Within these parameter ranges, we can obtain several options. We used the option with the lowest value of parameters to investigate the performance of the electromechanical diode in Figs. 9 and 10. The results in these figures demonstrate that the values of the transmission and asymmetric ratios are low at this wavelength

as compared to results at medium-wavelength limit (i.e., $k \sim \pi/2$). This is because the lowest values that were chosen to plot the figures resulted in an optical mode stretching over a narrow range of frequencies. Therefore, only a few frequency components with low energy content from the output wave (i.e., its frequency content is converted into frequencies other than the input frequency) can propagate through the narrow optical mode. To increase the frequency components that can propagate through the optical mode, the range of optical mode frequencies needs to be increased by choosing parameters with highest values among all available options. This can result in the widest possible optical mode within the above assumed system's parameters ranges. For this case, we plot the responses of the forward and backward configurations in Fig. 11. For hardening nonlinearity in the resonator at long-wavelength limit (i.e., $k \sim \pi/9$; Fig. 11(a)), the results indicate that the harvested voltage sensed at the other end is significantly higher than the case in Fig. 10(c). Yet, the wave cannot propagate in the backward configuration as depicted in Fig. 11(b). This can also be demonstrated from the values of transmission ratio $Tr_f \approx 0.1251$ and asymmetric ratio $\sigma \approx$ 1.5×10^6 , which are also significantly higher. Therefore, the performance of the nonlinear resonator electromechanical diode at the long-wavelength limit (i.e., $k \sim \pi/9$) is comparable to the performance of the nonlinear chain diode when the parameters of the linear chain are chosen carefully. Softening nonlinearity in the resonator with these linear chain parameters can even provide better performance, and thus higher voltage can be sensed at the other end (Fig. 11(c)), thus preventing any waves coming from the backward configuration from propagating through the structure (Fig. 11(d)). This observation is also confirmed by the values of transmission ratio $Tr_f \approx 0.49$ and asymmetric ratio $\sigma \approx 6.2 \times 10^6$, which are also significantly higher than the case of hardening nonlinearity.

Analyses in the current study are conducted on a chain of 500 cells (i.e., a nonlinear chain with 350 cells and a linear chain with 150 cells in the case of the electromechanical diode). However, it is crucial to shed light on the effect of the chain's length on the electromechanical diode performance. For an electromechanical diode consisting of a nonlinear chain with 50 cells coupled to a linear chain with 50 cells (Fig. 12(a)), the results indicate that the electromechanical diode can be operated in the case of shorter chains. However, for this case, the asymmetry ratio $\sigma = 19.63$ is significantly lower as compared to longer chains. To investigate the effect of length on the asymmetry ratio, we plot the asymmetry ratio for electromechanical diodes with different numbers of cells in Figs. 12(b)-12(d). First, we study an electromechanical diode with the number of cells in the nonlinear chain equal to the linear chain. We sweep the number of cells in each chain from 50 to 250 cells (i.e., in other words, we sweep the number of cells in the electromechanical diode from 100 cells to 500 cells) and plot the asymmetry ratio in Fig. 12(b). The results reveal that the asymmetry ratio at the order of 10⁵ can be obtained when each linear and nonlinear chain exceeds 170 cells. Next, we investigate the effect of the length of each chain (i.e., the linear and nonlinear chains) on the asymmetry ratio separately. First, we sweep the length of the nonlinear chain from 50 to 350 cells while fixing the length of the linear chain to 150 cells and plot the asymmetry ratios in Fig. 12(c). The results demonstrate that the asymmetry ratio is very sensitive to the length of the nonlinear chain. Asymmetry ratio at the order of 10⁵ can be obtained when the length of the nonlinear chain is greater than 170 cells. Next, we investigate the effect of the length of linear chain by sweeping the length of the linear chain from 50 to 150 cells while fixing the length of the nonlinear chain to 350 cells and plot the asymmetry ratio in Fig. 12(d). The results show that the length of the linear chain does not affect the asymmetry ratio significantly, unlike the length of the nonlinear chain. This observation further implies that a high asymmetry ratio can be obtained regardless of the length of the linear chain within the investigated range.

It is noteworthy that the output harvested voltage in the forward configuration appears at frequencies different than the input excitation frequency. This nonlinear frequency conversion may lead to a loss of information in the case of mechanical computing [61,62].

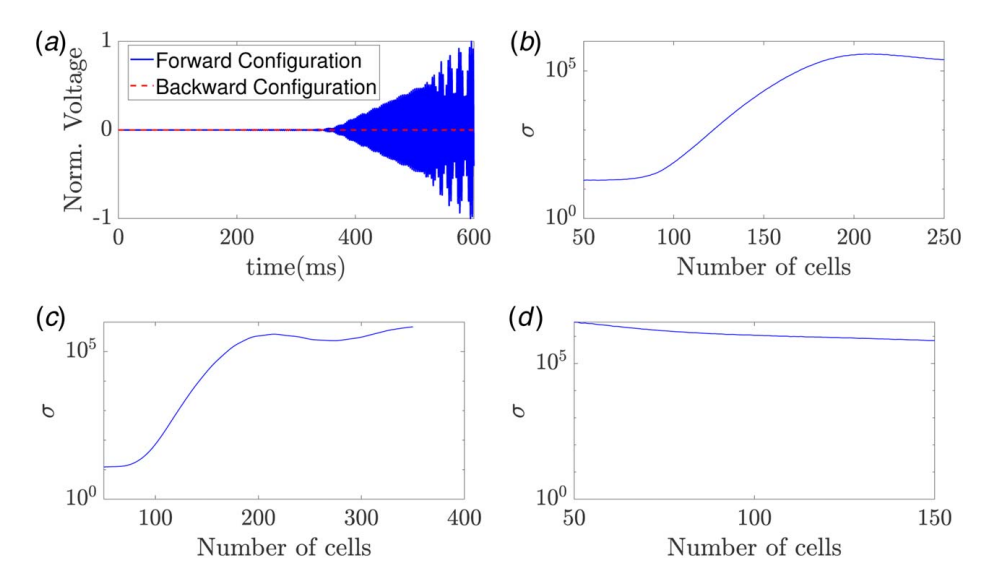


Fig. 12 The effect of chain's length on the asymmetry ratio; $\omega=2$, $\bar{k}_l=1.3$, $\bar{k}_p=0.16$, $\bar{m}_p=0.04$, $\varepsilon^2 A \alpha=0.03$, $\varepsilon^2 A \alpha_r=0$: (a) output voltage for electromechanical diode in the forward and backward configurations; each chain consists of 50 cells, (b) sweeping the number of cells in each chain from 50 to 250 cells, (c) sweeping the length of the nonlinear chain from 50 to 350 cells with fixing the length of the linear chain to 150 cells, and (d) sweeping the length of the linear chain from 50 to 150 cells with fixing the length of the nonlinear chain to 350 cells

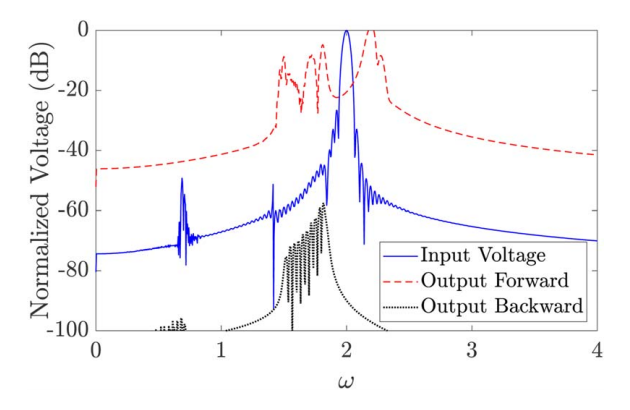


Fig. 13 Frequency spectra of the input and output signals in both configurations; $\omega=2$, $\bar{k}_{l}=1.3$, $\bar{k}_{p}=0.16$, $\bar{m}_{p}=0.04$, $\varepsilon^{2}A\alpha=0.03$, $\varepsilon^{2}A\alpha_{r}=0$

This can be demonstrated by plotting the frequency spectra of the input and output voltage for both configurations in Fig. 13. It can be observed that the output signal in the case of forward configuration appears at frequencies different than the input frequency spectrum. The output signal has a dip within the spectrum of the bandgap of the linear chain. Instead, the significant component appears at frequencies outside the linear chain's bandgap spectra. On the other hand, the output signal spectra have components with amplitudes significantly lower than the input signal amplitude. This is a clear indication that the wave cannot be propagated in the backward configuration.

6 The Effect of Linear Chain Bandgap Size on the Performance of the Electromechanical Diode

In the previous section, we demonstrated that the proposed electromechanical diode can be used as a direction-biased waveguide. This direction-biased waveguide can be operated in the medium-wavelength limit (i.e., $k \sim \pi/2$) for both nonlinear chain and nonlinear resonator cases, but the operation of this diode in the long-wavelength domain (i.e., $k \sim \pi/9$) is limited to the nonlinear resonator case only. It should be noted that the parameters of the linear

chain were chosen such that the bandgap of the linear chain is tuned to the operation frequency region to demonstrate the non-reciprocity. However, the effect of linear chain bandgap on the asymmetric ratio was not discussed in the previous section. Therefore, we present the asymmetric ratio for different linear chain's bandgap sizes and at different excitation frequencies.

In this section, we conduct our analyses by sweeping the bandgap size of the linear chain over either the whole frequency range of the nonlinear chain's optical mode frequencies or over a specific frequency range within the long-/medium-wavelength limits of the nonlinear chain's optical mode. In order to define the linear chain parameters that satisfy the tested bandgap size, we sweep the chain's parameters over the ranges defined in the previous section and pick the largest parameters of the list that matches the bandgap requirement.

6.1 Sweeping the Bandgap Over the Whole Optical Mode Frequencies. For sweep over the whole optical mode, we set the upper boundary of the bandgap to the maximum frequency in this mode and sweep the lower boundary over other frequencies in the optical mode in one case, and fix the lower boundary to the minimum frequency in this mode and sweep the upper in another case. For these two cases, we record the asymmetric ratio at different excitation frequencies and bandgap boundaries and plot them in Figs. 14 and 15, respectively.

For the case of lower boundary being swept over the whole range of the optical mode (Fig. 14), the electromechanical diode has the highest asymmetry ratio when the lower bandgap boundary is close to frequencies near the medium-wavelength limit (i.e., $k \sim \pi l$ 2) in the case of hardening chain nonlinearity as shown in Fig. 14(a). In particular, the medium-wavelength limit (i.e., $k \sim \pi l$ 2) is confined within the bandgap, and energy component associated with the shifted frequency can propagate through the passband below this bandgap. In addition, excitation frequencies near the medium-wavelength (i.e., $k \sim \pi/2$) show higher symmetry ratio where significant frequency shift can be observed as shown in the previous sections for this type of nonlinearity. When the lower bandgap boundary is below the medium-wavelength limit $(k \sim \pi l)$ 2) (i.e., in the long-wavelength limit $k \sim \pi/9$), the asymmetry ratio is very small and the electromechanical diode cannot be operated at all excitation frequencies within the optical mode. This is

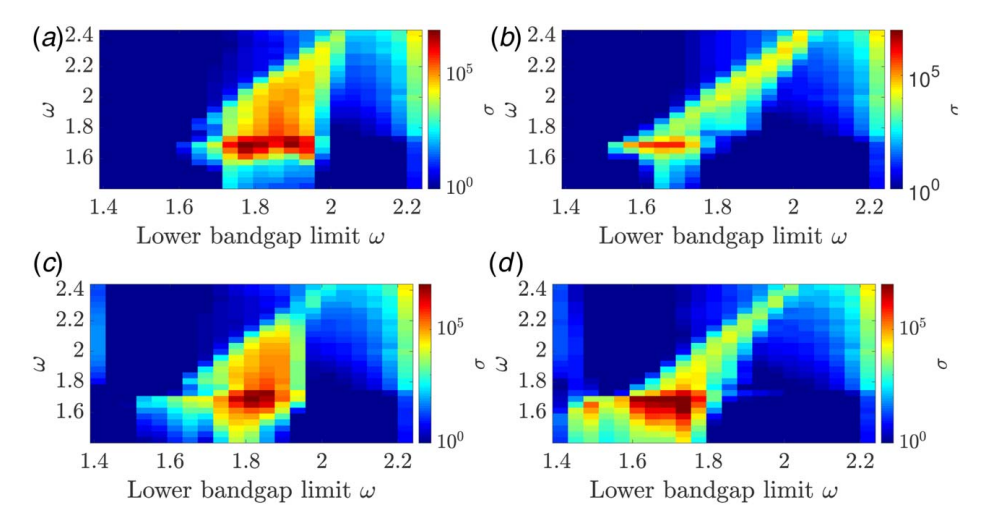


Fig. 14 Asymmetry ratio for different linear chain designs with bandgap tuned within the whole optical mode of nonlinear chain. Upper boundary of the bandgap is fixed to the maximum frequency of optical mode of nonlinear chain and lower limit is swept over the optical mode: (a) hardening nonlinear chain, $\varepsilon^2 A \alpha = 0.03$, $\varepsilon^2 A \alpha_r = 0$, (b) softening nonlinear chain, $\varepsilon^2 A \alpha = 0.03$, $\varepsilon^2 A \alpha_r = 0$, (c) hardening nonlinear resonator, $\varepsilon^2 A \alpha = 0$, $\varepsilon^2 A \alpha_r = 0.03$, and (d) softening nonlinear resonator, $\varepsilon^2 A \alpha = 0$, $\varepsilon^2 A \alpha_r = 0.03$.

because all shifted frequencies lie within the bandgap (i.e., the band covers most of the optical mode); therefore, no waves will propagate in either the forward or backward directions. By moving the lower bandgap boundary above the medium-wavelength limit (i.e., $k \sim \pi/2$), the asymmetry ratio becomes lower since the frequency shift becomes also less significant in the short-wavelength limit (i.e., $k \sim 7\pi/9$). In general, only excitation frequencies within the bandgap show directional-biased wave propagation for medium-/short-wavelength limits, while no frequencies show directional-biased wave propagation in the long-wavelength limit (i.e., $k \sim \pi/9$). For softening chain nonlinearity, similar observations can be deduced from Fig. 14(b). However, both excitation frequencies and lower bandgap boundary have high symmetric ratio at frequencies lower than the hardening case. This is not surprising, since results in Fig. 4(b) showed that the higher energy component is shifted below the medium-wavelength limit (i.e., $k \sim \pi/2$) in the case of softening chain nonlinearity, unlike the case of hardening nonlinearity. For hardening resonator nonlinearity (Fig. 14(c)),

the regions of high symmetry ratios are similar to those of hardening chain; however, these regions are slightly extended to cover the long-wavelength region (i.e., $k \sim \pi/9$). This indicates that the operation range of the electromechanical diode can be broadened using resonator nonlinearity. The operation range of the electromechanical diode can further be increased if softening nonlinearity is used as shown in Fig. 14(d), thus showing a good agreement with the observations in the previous section. Yet the significance of directional-biased wave propagation is not pronounced at this limit since the bandgap is tuned above this region due to fixing the higher bandgap boundary. Moreover, when the bandgap is tuned to this region, the bandgap covers most of the optical mode; therefore, the shifted frequency energy component cannot propagate in the forward configuration.

To obtain a bandgap that always covers the long-wavelength limit (i.e., $k \sim \pi/9$), we fix the lower bandgap boundary and sweep the upper boundary over the optical mode's frequencies. The asymmetry ratio for this case is shown in Fig. 15. For hardening chain

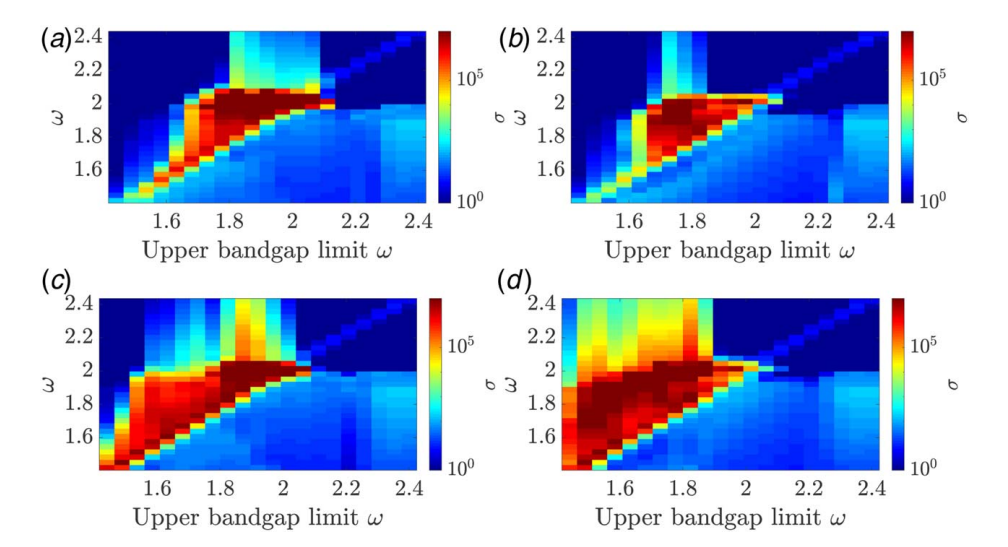


Fig. 15 Asymmetry ratio for different linear chain designs with bandgap tuned within the whole optical mode of nonlinear chain. Lower boundary of the bandgap is fixed to the maximum frequency of optical mode of nonlinear chain and upper limit is swept over the optical mode: (a) hardening nonlinear chain, $\varepsilon^2 A \alpha = 0.03$, $\varepsilon^2 A \alpha_r = 0$, (b) softening nonlinear chain, $\varepsilon^2 A \alpha = 0.03$, $\varepsilon^2 A \alpha_r = 0.03$, and (d) softening nonlinear resonator, $\varepsilon^2 A \alpha = 0$, $\varepsilon^2 A \alpha_r = 0.03$, and (d) softening nonlinear resonator, $\varepsilon^2 A \alpha = 0$, $\varepsilon^2 A \alpha_r = 0.03$.

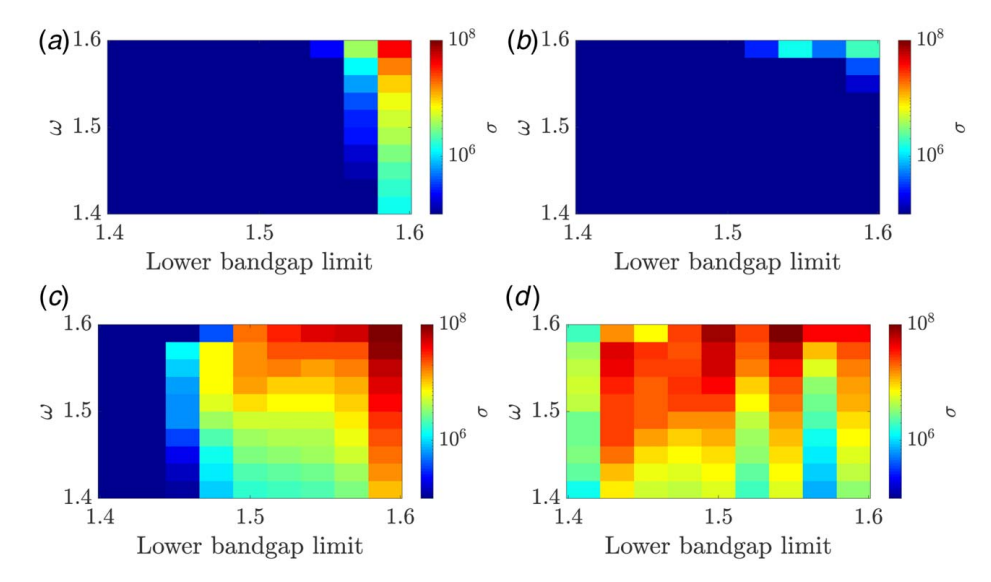


Fig. 16 Asymmetry ratio for different linear chain designs with bandgap tuned within the long wavelength limit in the optical mode of nonlinear chain. Upper boundary of the bandgap is fixed to $\omega=1.9$ optical mode of nonlinear chain and lower limit is swept over the long-wavelength limit in the optical mode: (a) hardening nonlinear chain, $\varepsilon^2 A \alpha = 0.03$, $\varepsilon^2 A \alpha_r = 0$, (b) softening nonlinear chain, $\varepsilon^2 A \alpha = -0.03$, $\varepsilon^2 A \alpha_r = 0$, (c) hardening nonlinear resonator, $\varepsilon^2 A \alpha = 0$, $\varepsilon^2 A \alpha_r = 0.03$, and (d) softening nonlinear resonator, $\varepsilon^2 A \alpha = 0$, $\varepsilon^2 A \alpha_r = 0.03$.

(Fig. 15(a)), the results indicate that with increasing the excitation frequency to get closer to the medium-wavelength limit (i.e., $k \sim$ $\pi/2$), energy contents with shifted frequency components start to appear and directional-biased wave transmission can be observed. Yet the asymmetry ratio is not significant in the long-wavelength limit (i.e., $k \sim \pi/9$) and starts to increase rapidly as excitation frequencies approach the medium-wavelength limit (i.e., $k \sim \pi/2$) and the bandgap covers this wavelength limit. It is noteworthy that the transmission ratios are higher in this case, which indicates that the frequency conversion shifts the signal frequency to a frequency above the bandgap and a significant energy content is associated with these shifted high frequencies. Consequently, the upper bandgap boundary should be restricted to below short-wavelength $(k \sim 7\pi/9)$ region (just above frequencies within mediumwavelength limit (i.e., $k \sim \pi/2$), since a significant portion of the energy is shifted to the long-wavelength limit (i.e., $k \sim \pi/9$)) for higher asymmetry ratio in designing linear chains. These observations also hold for the softening chain case, as shown in Fig. 15(b). However, the asymmetry ratio is lower at high frequencies since frequency conversion tends to shift the excitation frequencies to lower frequencies which lie within the bandgap, thus the transmitted energy is lower. For hardening resonator, Fig. 15(c) shows a significant increase in the asymmetry ratio near the long-wavelength limit (i.e., $k \sim \pi/9$) as compared with cases in Figs. 15(a) and 15(b). Yet high asymmetry ratios can still be observed in the medium-wavelength limit (i.e., $k \sim \pi/2$). In addition, the values of asymmetry ratios are significantly higher than the case of sweeping lower bandgap limit since the bandgap can cover the medium-/long-wavelength limits with passband for frequencies at short-wavelength limit (i.e., $k \sim 7\pi/9$). This increase in asymmetry ratio becomes more pronounced with softening resonators, as shown in Fig. 15(d). For the nonlinear resonator case, the directional-biased wave propagation can even be observed at high excitation frequencies where frequency components can also be shifted, as seen in Figs. 15(c) and 15(d). However, the asymmetry ratio here is lower than other frequencies within medium-/longwavelengths limits. Finally, it is noteworthy that the asymmetry ratios are higher when sweeping the upper bandgap boundary, as compared to sweeping the lower boundary, since the shortwavelength limit (i.e., $k \sim 7\pi/9$) is a passband in most cases where shifted excitation frequencies can propagate.

Based on the above discussions, the bandgap of the linear chain should not intersect with the long-/medium-wavelength frequencies if the operation frequencies are confined within the short-wavelength limit (i.e., $k \sim 7\pi/9$). Moreover, the bandgap of the linear chain should not intersect with the short-wavelength frequencies if the operation frequencies are confined within the long-/medium-wavelength limits. These considerations should be considered when designing an electromechanical diode. Furthermore, it is more beneficial to design the diode for operation range within the long-/medium-wavelength limits since the asymmetry ratios are much higher in these regions as compared to the short-wavelength limit (i.e., $k \sim 7\pi/9$). After reaching a conclusion about avoiding tuning the bandgap to the short-wavelength limit (i.e., $k \sim 7\pi/9$) due to low asymmetry ratio, we should conduct a deeper investigation about tuning the bandgap to the long-/medium-wavelength limits.

6.2 Sweeping the Bandgap Over the Long-Wavelength Limit Optical Mode Frequencies. In this section, we conduct further analyses to sweep the boundaries of the linear chain's bandgap over the long-wavelength (i.e., $k \sim \pi/9$) and mediumwavelength (i.e., $k \sim \pi/2$) limits separately. This can be done by conducting analyses similar to those conducted in Figs. 14 and 15. In particular, we fix the upper boundary (of the linear chain's bandgap) and sweep the lower boundary in one case (Fig. 16), while we fix the lower boundary and sweep the upper boundary in another (Fig. 17). For analyses over the long-wavelength frequencies (i.e., $k \sim \pi/9$) while fixing the bandgap's upper boundary, we plot the results in Fig. 16. For hardening and softening chains (Figs. 16(a) and 16(b)), the results indicate that the asymmetry ratio is almost zero for all lower bandgap boundaries. However, the asymmetry ratio can be non-zero when the lower bandgap boundary is near the medium-wavelength limit (i.e., $k \sim \pi/2$), where the nonlinear chain shows direction-biased wave propagation. In addition, the asymmetry ratio is higher for the case of hardening chain. On the other hand, the nonlinearity in the resonator shows a high asymmetry ratio for all lower bandgap boundaries at all excitation frequencies within this limit, as shown in Figs. 16(c) and 16(d). Nevertheless, the lower bandgap boundary does not need to cover frequencies ($\omega \le 1.48$) since the asymmetry

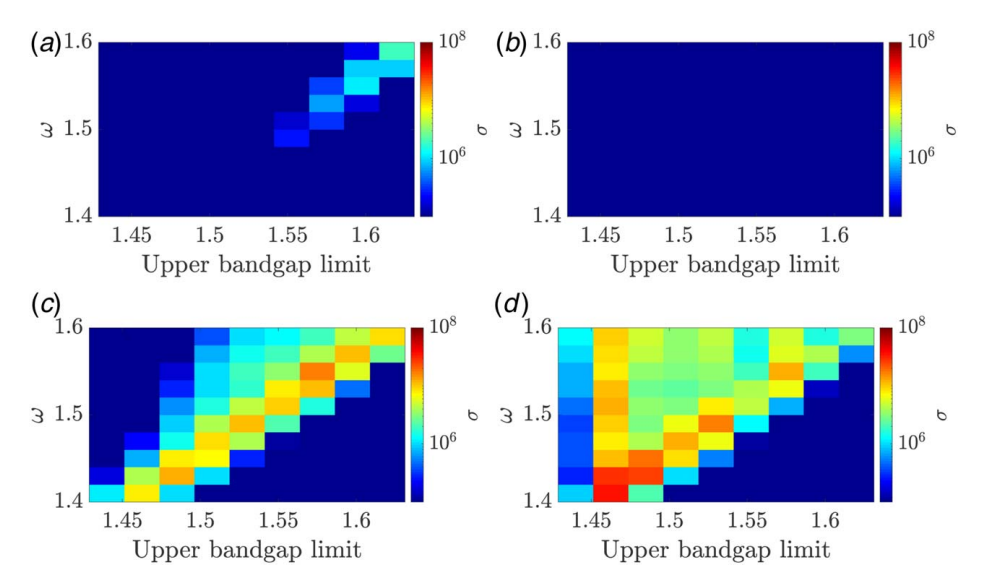


Fig. 17 Asymmetry ratio for different linear chain designs with bandgap tuned within the long wavelength limit in the optical mode of nonlinear chain. Lower boundary of the bandgap is fixed to $\omega=1.4$ optical mode of nonlinear chain and upper limit is swept over the long-wavelength limit in the optical mode: (a) hardening nonlinear chain, $\varepsilon^2 A \alpha = 0.03$, $\varepsilon^2 A \alpha_r = 0$, (b) softening nonlinear chain, $\varepsilon^2 A \alpha = 0.03$, $\varepsilon^2 A \alpha_r = 0$, (c) hardening nonlinear resonator, $\varepsilon^2 A \alpha = 0$, $\varepsilon^2 A \alpha_r = 0.03$, and (d) softening nonlinear resonator, $\varepsilon^2 A \alpha = 0$, $\varepsilon^2 A \alpha_r = 0.03$.

ratio is very low in this region for the case of hardening resonator, as shown in Fig. 16(c). However, the lower boundary can be extended to cover this region of frequencies in the case of softening resonator, as shown in Fig. 16(d). For the case of the lower bandgap boundary being fixed, the results also show approximately zero asymmetry ratio in the cases of hardening and softening chain, as shown in Figs. 17(a) and 17(b). In addition, sweeping the upper limit in this case is associated with lower asymmetry ratios for frequencies near the medium-wavelength limit (i.e., $k \sim \pi/2$) as compared to the previous case shown in Figs. 16(a) and 16(b). For hardening and softening resonators (Figs. 16(c) and 16(d)), high asymmetry ratios exist in the region on and above the diagonal (i.e., excitation frequency/upper bandgap boundary) line unlike the case of fixing the upper bandgap boundary where higher asymmetry ratios can

be observed at wider range of excitation frequencies. This indicates that fixing the upper bandgap boundary is more beneficial than fixing the lower boundary. Therefore, when designing an electromechanical diode that shows high asymmetry ratio in the long-wavelength limit (i.e., $k \sim \pi/9$), the upper bandgap's boundary should be tuned to a frequency near the lower frequencies within the medium-wavelength limit (i.e., $k \sim \pi/2$). On the other hand, the lower bandgap's boundary should be tuned to a frequency just above the lower frequencies within the optical mode in the presence of resonator nonlinearity.

6.3 Sweeping the Bandgap Over the Medium-Wavelength Optical Mode Frequencies. Similarly, we focus on the sweep of the linear chain bandgap's boundaries inside the medium-

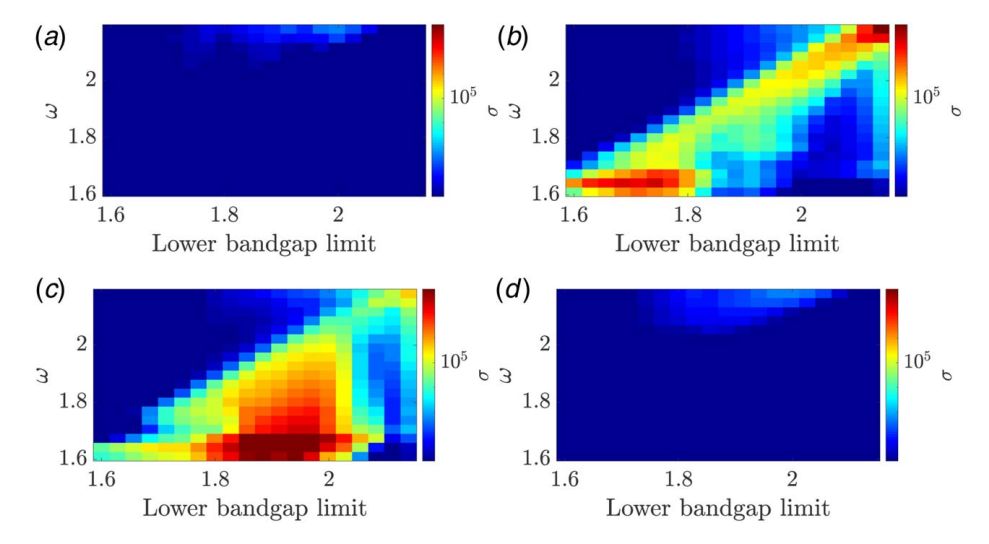


Fig. 18 Asymmetry ratio for different linear chain designs with bandgap tuned within the medium-wavelength limit (i.e., $k \sim \pi/2$) in the optical mode of nonlinear chain. Upper boundary of the bandgap is fixed to $\omega = 2.2$ optical mode of nonlinear chain and lower limit is swept over the medium-wavelength limit (i.e., $k \sim \pi/2$) in the optical mode: (a) hardening nonlinear chain, $\varepsilon^2 A \alpha = 0.03$, $\varepsilon^2 A \alpha_r = 0$, (b) softening nonlinear chain, $\varepsilon^2 A \alpha = -0.03$, $\varepsilon^2 A \alpha_r = 0$, (c) hardening nonlinear resonator, $\varepsilon^2 A \alpha = 0$, $\varepsilon^2 A \alpha_r = 0.03$, and (d) softening nonlinear resonator, $\varepsilon^2 A \alpha = 0$, $\varepsilon^2 A \alpha_r = 0.03$.

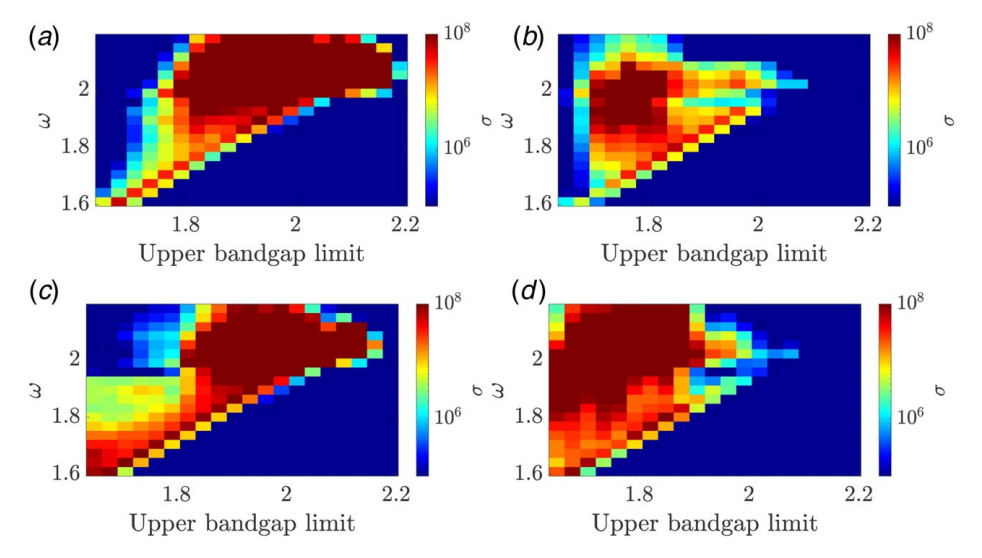


Fig. 19 Asymmetry ratio for different linear chain designs with bandgap tuned within the medium-wavelength limit (i.e., $k \sim \pi/2$) in the optical mode of nonlinear chain. Lower boundary of the bandgap is fixed to $\omega=1.9$ optical mode of nonlinear chain and upper limit is swept over the medium-wavelength limit (i.e., $k \sim \pi/2$) in the optical mode: (a) hardening nonlinear chain, $\varepsilon^2 A \alpha = 0.03$, $\varepsilon^2 A \alpha_r = 0$, (b) softening nonlinear chain, $\varepsilon^2 A \alpha = -0.03$, $\varepsilon^2 A \alpha_r = 0$, (c) hardening nonlinear resonator, $\varepsilon^2 A \alpha = 0$, $\varepsilon^2 A \alpha_r = 0.03$, and (d) softening nonlinear resonator, $\varepsilon^2 A \alpha = 0$, $\varepsilon^2 A \alpha_r = 0.03$.

wavelength limit (i.e., $k \sim \pi/2$) and plot the results in Figs. 18 and 19. For fixed upper bandgap boundary, the results indicate that the asymmetry ratio is almost zero for hardening chain (Fig. 18(a)) and softening resonator (Fig. 18(d)). However, the asymmetry ratio has significant values for softening chain (Fig. 18(c)) and hardening resonator (Fig. 18(d)). On the other hand, fixing the lower bandgap's boundary reveals significantly higher asymmetry ratio, as shown in Fig. 19. In particular, in the case of hardening chain (Fig. 19(a)), the asymmetry ratio is significantly higher as compared to the case of sweeping the lower bandgap's boundary for this type of nonlinearity. Similarly, the asymmetry ratio is higher for the case of softening chain, as shown in Fig. 19(b). However, the results indicate that sweeping the upper boundary shows higher asymmetry ratio at high frequencies as compared to the case of sweeping the lower boundary where high asymmetry is associated with low frequencies. For the case of resonator nonlinearity (Figs. 19(c) and 19(d)), we observe that fixing the lower limit results in high asymmetry ratio at higher excitation frequencies within the medium-wavelength limit (i.e., $k \sim \pi/2$) as compared to fixing the upper boundary. It is noteworthy that hardening nonlinearity provides high asymmetry ratio when the upper bandgap's boundary is close to the upper end of the medium-wavelength limit's (i.e., $k \sim \pi/2$) frequencies since signals tend to be shifted to higher frequencies with hardening nonlinearity. The opposite is observed when we set the upper bandgap's boundary to a frequency below the higher frequencies of the medium-wavelength limit (i.e., $k \sim \pi/2$). This is because signals tend to be shifted to lower frequencies with softening nonlinearity.

The above analyses provide some guidelines for designing the linear chain in the electromechanical diode. The design guidelines depend on the operation frequency of the electromechanical diode and the type of nonlinearity. General guidelines include avoiding tuning the bandgap to short-wavelength limit to allow shifted frequency components to propagate in the forward direction. In addition, the lower boundary should be fixed just above the lowest frequency in the optical mode for best performance at frequencies within the long-wavelength limit and resonator nonlinearity should be used. For this operation range, the upper limit should be set near the lower end of the medium-wavelength limit. Moreover, the lower boundary should be tuned just below the medium-wavelength limit for best performance at frequencies within the medium-wavelength limit and either resonator or chain nonlinearity can be

used. The upper boundary should be placed at the end of the mediumwavelength in the case of hardening nonlinearity and slightly below the short-wavelength limit in the case of softening nonlinearity.

The realized electromechanical diode in the current study (harvesting energy only in one way) can be useful in designing mechanical circuits and mechanical logic gates. These novel elastoacoustics devices can also be employed in mechanical computing [62]. Although mechanical computing may not replace the current electronics conventional computing, it can augment electronics computing due to its ability to process information through interacting and adapting to the environment. This can be achieved through the study of digital logic/diodes in mechanical computing. These mechanical logic gates/diodes can advance multibit logic circuits [63], communication (i.e., since optical waves are quickly dissipated in mediums other than air, elastic and acoustics communication can be advanced by mechanical computing) [64], thus improving ultrasound imaging/therapy [65], non-destructive testing [66,67], sensing [68], and signal processing [62,69].

With advances in additive manufacturing and metamaterial designs, the investigated electromechanical diode may be verified experimentally. In particular, studies in the literature indicated that nonlinear locally resonant metamaterials (with resonator nonlinearity) can be fabricated based on geometric nonlinearity using standard electrical discharge machining [70]. Coupling this nonlinear metastructure to a linear metastructure and installing energy harvesters on the linear and nonlinear resonators can lead to the fabrication of the proposed diode. Then, the fabricated structure can be tested to demonstrate the observed phenomena experimentally. However, this is beyond the scope of the current study and left for future work.

7 Conclusion

In this paper, a nonlinear metamaterial with electromechanical local resonators was investigated for the purpose of designing a broadband electromechanical diode. The nonlinearity stemmed from the chain in one case and from the resonator in another. The method of multiple scales was applied to the governing equations of motion to obtain the dispersion relations. The analytical band structure was validated via comparison with results obtained by direct numerical integration. The results show good agreement except that the analytical results fail to predict some frequency

regions within the optical mode due to significant frequency shift, in particular the medium-wavelength limit for the case of nonlinear chain and the long-/medium-wavelength limit for the nonlinear resonator. To further demonstrate the frequency shift in these regions, we analyzed the numerical results by spectro-spatial analysis. The spatial profiles indicated that the wave is severely distorted in these regions and may split into localized and dispersive waves. Moreover, the spectrograms and contour plots of 2D FFT demonstrated that most of the energy content of the output voltage appears at frequencies outside the initial frequency band of the input signal. The observed significant frequency shift was utilized to design an electromechanical direction-biased waveguide (i.e., electromechanical diode). The proposed electromechanical diode was constructed by combining linear and nonlinear chains with electromechanical local resonators. This diode showed the ability to harvest energy and sense the wave propagating in the forward direction only, and blocked any wave propagating in the backward configuration. This direction-biased wave propagation can be observed only at the medium-wavelength limit in the case of nonlinear chain. However, it can be observed at the medium-/longwavelength limits in the case of nonlinear resonator. Therefore, the electromechanical diode can be operated over a wider range of frequencies in the case of nonlinear resonator. Unlike mechanical diodes in the literature, the proposed diode does not only have a high asymmetry ratio, it also has a high transmission ratio for the forward configuration. Yet the proposed electromechanical diode can harvest energy and sense better than symmetric systems due to the birth of localized (solitary) waves. To draw guidelines on designing the linear chain's bandgap, we conducted analyses by sweeping the bandgap's boundaries over different frequency ranges and reported the asymmetry ratio of these simulations. The results indicated that it is more beneficial to tune the lower bandgap's boundary just above the minimum frequency of the optical mode of the nonlinear chain and fix the upper bandgap's boundary near the medium-wavelength limit for best performance in the longwavelength limit for the case of nonlinear resonator. In addition, softening resonator should be used to realize high asymmetry ratio at low frequencies in the optical mode. Moreover, the results demonstrated that the lower bandgap's boundary should be tuned just above the long-wavelength limit to obtain high asymmetry ratio for excitation frequencies within the medium-wavelength limit for both types of nonlinearity. On the other hand, the results indicated that the upper bandgap's boundary should not go into the short-wavelength limit's frequencies and should be fixed

slightly lower in the case of softening nonlinearity. Finally, the bandgap's boundaries should be tuned around the operation frequency, in general, and extending its size to the short-wavelength region should be avoided to allow shifted frequency component to propagate in the forward configuration.

Acknowledgment

This work is supported in part by the National Science Foundation (NSF) Grant CMMI-2038187.

Conflict of Interest

There are no conflicts of interest.

Data Availability Statement

The datasets generated and supporting the findings of this article are obtainable from the corresponding author upon reasonable request.

Appendix

In order to determine the nonlinear frequency correction coefficient b', the solvability condition needs to be solved to eliminate secular unbounded terms. After some algebric manipulation, the values of g, h, l, f for the case of nonlinear chain can be expressed as

$$g = -\frac{1}{2}\omega(\alpha_2\omega(\Omega_0^2(\bar{k}(\alpha_1(-\operatorname{Im}[\Gamma]\operatorname{Im}[K_\omega] + (\alpha_1\operatorname{Re}[\Gamma] - 2)\operatorname{Re}[K_\omega] - 2) + 2\omega^2) - 2) + 2\Omega_0^2\bar{k}\operatorname{Im}[K_\omega] - \alpha_1\alpha_3\omega(\Omega_0^2\bar{k}(\operatorname{Re}[K_\omega] + 2) + 2)))$$

$$h = \frac{1}{2}\omega(\Omega_0^2(\bar{k}(\operatorname{Re}[K_\omega](\alpha_1\alpha_2\operatorname{Im}[\Gamma]\omega - 2) + \omega\operatorname{Im}[K_\omega](\alpha_2(\alpha_1\operatorname{Re}[\Gamma] - 2) - \alpha_1\alpha_3) - 2) + 2\omega^2) - 2)$$

$$f = \frac{3}{2}\alpha(1 - \cos k)(\omega^2\Omega_0^2 - 1)$$
(A1)

$$l = \frac{1}{2}(-3)\alpha(1 - \cos k)\omega(\alpha_2(\omega^2\Omega_0^2 - 1) - \alpha_1\alpha_3)$$
 (A2)

while for the case of nonlinear resonator, these values can be expressed as

$$g = -\frac{1}{2}\omega\left(\alpha_2\omega\left(\Omega_0^2\left(\bar{k}\left(\alpha_1(-\mathrm{Im}[\Gamma])\mathrm{Im}[K_\omega] + \left(\alpha_1\mathrm{Re}[\Gamma] - 2\right)\mathrm{Re}[K_\omega] - 2\right) + 2\omega^2\right) - 2\right) + 2\Omega_0^2\bar{k}\mathrm{Im}[K_\omega] - \alpha_1\alpha_3\omega\left(\Omega_0^2\bar{k}\left(\mathrm{Re}[K_\omega] + 2\right) + 2\right)\right) \tag{A3}$$

$$h = \frac{1}{2}\omega\left(\Omega_0^2\left(\bar{k}\left(\operatorname{Re}[K_\omega]\left(\alpha_1\alpha_2\operatorname{Im}[K_\omega]\omega - 2\right) + \omega\operatorname{Im}[K_\omega]\left(\alpha_2\left(\alpha_1\operatorname{Re}[\Gamma] - 2\right) - \alpha_1\alpha_3\right) - 2\right) + 2\omega^2\right) - 2\right)$$
(A4)

$$f = \frac{3}{8} \gamma^3 \alpha \omega^2 \Omega_0^2 \bar{k} \left(\alpha_2 \omega \operatorname{Im}[K_{\omega}]^3 - 3\alpha_2 \omega \operatorname{Im}[K_{\omega}] \operatorname{Re}[K_{\omega}]^2 + 3\operatorname{Im}[K_{\omega}]^2 \operatorname{Re}[K_{\omega}] - \operatorname{Re}[K_{\omega}]^3 \right)$$
(A5)

$$l = \frac{1}{8}(-3)\gamma^3\alpha\omega^2\Omega_0^2\bar{k}\left(3\alpha_2\omega\operatorname{Im}[K_\omega]^2\operatorname{Re}[K_\omega] + 3\operatorname{Im}[K_\omega]\operatorname{Re}[K_\omega]^2 - \operatorname{Im}[K_\omega]^3 - \alpha_2\omega\operatorname{Re}[K_\omega]^3\right) \tag{A6}$$

It is noteworthy that in the presence of both nonlinearities (i.e., chain and resonator nonlinearities), the nonlinear frequency correction coefficient can be written as

$$\beta' = \beta'_{ch} + \beta'_{res} \tag{A7}$$

where β'_{ch} is the correction coefficient for the case of nonlinear chain case and β'_{res} is the correction coefficient for the nonlinear resonator case.

References

- Hussein, M. I., Leamy, M. J., and Ruzzene, M., 2014, "Dynamics of Phononic Materials and Structures: Historical Origins, Recent Progress, and Future Outlook," Appl. Mech. Rev., 66(4), p. 040802.
- [2] Bertoldi, K., Vitelli, V., Christensen, J., and van Hecke, M., 2017, "Flexible Mechanical Metamaterials," Nat. Rev. Mater., 2(11), p. 17066.
 [3] Sigalas, M. M., and Economou, E. N., 1992, "Elastic and Acoustic Wave Band
- [3] Sigalas, M. M., and Economou, E. N., 1992, "Elastic and Acoustic Wave Bane Structure," J. Sound Vib., 158(2), pp. 377–382.
- [4] Sigalas, M., and Economou, E. N., 1993, "Band Structure of Elastic Waves in Two Dimensional Systems," Solid State Commun., 86(3), pp. 141–143.

- [5] Kushwaha, M. S., Halevi, P., Dobrzynski, L., and Djafari-Rouhani, B., 1993, "Acoustic Band Structure of Periodic Elastic Composites," Phys. Rev. Lett., 71(13), p. 2022.
- [6] Kushwaha, M. S., Halevi, P., Martinez, G., Dobrzynski, L., and Djafari-Rouhani, B., 1994, "Theory of Acoustic Band Structure of Periodic Elastic Composites," Phys. Rev. B, 49(4), p. 2313.
- [7] Vasseur, J., Djafari-Rouhani, B., Dobrzynski, L., Kushwaha, M., and Halevi, P., 1994, "Complete Acoustic Band Gaps in Periodic Fibre Reinforced Composite Materials: The Carbon/Epoxy Composite and Some Metallic Systems," J. Phys.: Condens. Matter, 6(42), p. 8759.
- [8] Kushwaha, M. S., 1996, "Classical Band Structure of Periodic Elastic Composites," Int. J. Mod. Phys. B, 10(9), pp. 977–1094.
- [9] Liu, Z., Zhang, X., Mao, Y., Zhu, Y., Yang, Z., Chan, C. T., and Sheng, P., 2000, "Locally Resonant Sonic Materials," Science, 289(5485), pp. 1734–1736.
- [10] Achaoui, Y., Laude, V., Benchabane, S., and Khelif, A., 2013, "Local Resonances in Phononic Crystals and in Random Arrangements of Pillars on a Surface," J. Appl. Phys., 114(10), p. 104503.
- [11] Liu, L., and Hussein, M. I., 2012, "Wave Motion in Periodic Flexural Beams and Characterization of the Transition Between Bragg Scattering and Local Resonance," ASME J. Appl. Mech., 79(1), p. 011003.
- [12] Manimala, J. M., and Sun, C., 2016, "Numerical Investigation of Amplitude-Dependent Dynamic Response in Acoustic Metamaterials With Nonlinear Oscillators," J. Acoust. Soc. Am., 139(6), pp. 3365–3372.
- [13] Kivshar, Y. S., and Flytzanis, N., 1992, "Gap Solitons in Diatomic Lattices," Phys. Rev. A, 46(12), p. 7972.
- [14] Nadkarni, N., Daraio, C., and Kochmann, D. M., 2014, "Dynamics of Periodic Mechanical Structures Containing Bistable Elastic Elements: From Elastic to Solitary Wave Propagation," Phys. Rev. E, 90(2), p. 023204.
- [15] Liang, B., Yuan, B., and Cheng, J.-C., 2009, "Acoustic Diode: Rectification of Acoustic Energy Flux in One-Dimensional Systems," Phys. Rev. Lett., 103(10), p. 104301.
- [16] Bukhari, M., and Barry, O., 2020, "Simultaneous Energy Harvesting and Vibration Control in a Nonlinear Metastructure: A Spectro-Spatial Analysis," J. Sound Vib., 473, p. 115215.
- [17] Nayfeh, A. H., 2011, Introduction to Perturbation Techniques, John Wiley & Sons, New York.
- [18] Nayfeh, A. H., and Mook, D. T., 2008, Nonlinear Oscillations, John Wiley & Sons, New York.
- [19] Narisetti, R. K., Leamy, M. J., and Ruzzene, M., 2010, "A Perturbation Approach for Predicting Wave Propagation in One-Dimensional Nonlinear Periodic Structures," ASME J. Vib. Acoust., 132(3), p. 031001.
- [20] Zhou, W., Li, X., Wang, Y., Chen, W., and Huang, G., 2018, "Spectro-Spatial Analysis of Wave Packet Propagation in Nonlinear Acoustic Metamaterials," J. Sound Vib., 413, pp. 250–269.
- [21] Bukhari, M., and Barry, O., 2020, "Spectro-Spatial Analyses of a Nonlinear Metamaterial With Multiple Nonlinear Local Resonators," Nonlinear Dyn., 99(2), pp. 1539–1560.
- [22] Khajehtourian, R., and Hussein, M. I., 2014, "Dispersion Characteristics of a Nonlinear Elastic Metamaterial," AIP Adv., 4(12), p. 124308.
- [23] Abedin-Nasab, M. H., Bastawrous, M. V., and Hussein, M. I., 2020, "Explicit Dispersion Relation for Strongly Nonlinear Flexural Waves Using the Homotopy Analysis Method," Nonlinear Dyn., 99(1), pp. 737–752.
- [24] Ganesh, R., and Gonella, S., 2013, "Spectro-Spatial Wave Features as Detectors and Classifiers of Nonlinearity in Periodic Chains," Wave Motion, 50(4), pp. 821–835.
- [25] Bukhari, M. A., and Barry, O. R., 2019, "On the Spectro-Spatial Wave Features in Nonlinear Metamaterials With Multiple Local Resonators," ASME 2019 International Design Engineering Technical Conferences and Computers and Information in Engineering Conference, Anaheim, CA, Aug. 18.
- [26] Bukhari, M., and Barry, O., 2020, "Nonlinear Metamaterials with Multiple Local Mechanical Resonators: Analytical and Numerical Analyses," New Trends in Nonlinear Dynamics, W. Lacarbonara, B. Balachandran, J. Ma, J. A. Tenreiro Machado, and G. Stepan, eds., Springer, Cham, pp. 13–21.
- [27] Thorp, O., Ruzzene, M., and Baz, A., 2001, "Attenuation and Localization of Wave Propagation in Rods With Periodic Shunted Piezoelectric Patches," Smart Mater. Struct., 10(5), p. 979.
- [28] Airoldi, L., and Ruzzene, M., 2011, "Wave Propagation Control in Beams Through Periodic Multi-branch Shunts," J. Intell. Mater. Syst. Struct., 22(14), pp. 1567–1579.
- [29] Casadei, F., Delpero, T., Bergamini, A., Ermanni, P., and Ruzzene, M., 2012, "Piezoelectric Resonator Arrays for Tunable Acoustic Waveguides and Metamaterials," J. Appl. Phys., 112(6), p. 064902.
- [30] Bergamini, A., Delpero, T., Simoni, L. D., Lillo, L. D., Ruzzene, M., and Ermanni, P., 2014, "Phononic Crystal With Adaptive Connectivity," Adv. Mater., 26(9), pp. 1343–1347.
- [31] Zhou, W., Wu, Y., and Zuo, L., 2015, "Vibration and Wave Propagation Attenuation for Metamaterials by Periodic Piezoelectric Arrays With High-Order Resonant Circuit Shunts," Smart Mater. Struct., 24(6), p. 065021.
- [32] Hu, G., Tang, L., Banerjee, A., and Das, R., 2017, "Metastructure With Piezoelectric Element for Simultaneous Vibration Suppression and Energy Harvesting," ASME J. Vib. Acoust., 139(1), p. 011012.
- [33] Hu, G., Tang, L., and Das, R., 2017, "Metamaterial-Inspired Piezoelectric System With Dual Functionalities: Energy Harvesting and Vibration Suppression," Active and Passive Smart Structures and Integrated Systems, Portland, OR, Apr. 11, SPIE, p. 101641X.

- [34] Hu, G., Tang, L., and Das, R., 2018, "Internally Coupled Metamaterial Beam for Simultaneous Vibration Suppression and Low Frequency Energy Harvesting," J. Appl. Phys., 123(5), p. 055107.
- [35] Shen, L., Wu, J. H., Zhang, S., Liu, Z., and Li, J., 2015, "Low-Frequency Vibration Energy Harvesting Using a Locally Resonant Phononic Crystal Plate With Spiral Beams," Mod. Phys. Lett. B, 29(1), p. 1450259.
- [36] Li, Y., Baker, E., Reissman, T., Sun, C., and Liu, W. K., 2017, "Design of Mechanical Metamaterials for Simultaneous Vibration Isolation and Energy Harvesting," Appl. Phys. Lett., 111(25), p. 251903.
- [37] Bukhari, M. A., Qian, F., Barry, O. R., and Zuo, L., 2020, "Effect of Electromechanical Coupling on Locally Resonant Metastructures for Simultaneous Energy Harvesting and Vibration Attenuation Applications," ASME 2020 Dynamic Systems and Control Conference, Online, Oct. 5, American Society of Mechanical Engineers.
- [38] Nassar, H., Yousefzadeh, B., Fleury, R., Ruzzene, M., Alù, A., Daraio, C., Norris, A. N., Huang, G., and Haberman, M. R., 2020, "Nonreciprocity in Acoustic and Elastic Materials," Nat. Rev. Mater., 5(9), pp. 667–685.
- [39] Fleury, R., Sounas, D. L., Sieck, C. F., Haberman, M. R., and Alù, A., 2014, "Sound Isolation and Giant Linear Nonreciprocity in a Compact Acoustic Circulator," Science, 343(6170), pp. 516–519.
- [40] Zangeneh-Nejad, F., and Fleury, R., 2018, "Doppler-Based Acoustic Gyrator," Appl. Sci., 8(7), p. 1083.
- [41] Nassar, H., Chen, H., Norris, A., and Huang, G., 2017, "Non-reciprocal Flexural Wave Propagation in a Modulated Metabeam," Extreme Mech. Lett., 15, pp. 97– 102
- [42] Nassar, H., Chen, H., Norris, A., and Huang, G., 2018, "Quantization of Band Tilting in Modulated Phononic Crystals," Phys. Rev. B, 97(1), p. 014305.
- [43] Trainiti, G., and Ruzzene, M., 2016, "Non-reciprocal Elastic Wave Propagation in Spatiotemporal Periodic Structures," New J. Phys., 18(8), p. 083047.
- [44] Wang, Y., Yousefzadeh, B., Chen, H., Nassar, H., Huang, G., and Daraio, C., 2018, "Observation of Nonreciprocal Wave Propagation in a Dynamic Phononic Lattice," Phys. Rev. Lett., 121(19), p. 194301.
- [45] Chen, Y., Li, X., Nassar, H., Norris, A. N., Daraio, C., and Huang, G., 2019, "Nonreciprocal Wave Propagation in a Continuum-Based Metamaterial With Space-Time Modulated Resonators," Phys. Rev. Appl., 11(6), p. 064052.
- [46] Nassar, H., Xu, X., Norris, A., and Huang, G., 2017, "Modulated Phononic Crystals: Non-reciprocal Wave Propagation and Willis Materials," J. Mech. Phys. Solids, 101, pp. 10–29.
- [47] Chen, H., Yao, L., Nassar, H., and Huang, G., 2019, "Mechanical Quantum Hall Effect in Time-Modulated Elastic Materials," Phys. Rev. Appl., 11(4), p. 044029.
- [48] Nash, L. M., Kleckner, D., Read, A., Vitelli, V., Turner, A. M., and Irvine, W. T., 2015, "Topological Mechanics of Gyroscopic Metamaterials," Proc. Natl. Acad. Sci. U.S.A., 112(47), pp. 14495–14500.
- [49] Zheng, Y., Zhang, J., Qu, Y., and Meng, G., 2021, "Adaptive Nonreciprocal Wave Attenuation in Linear Piezoelectric Metastructures Shunted With One Way Flootrical Transmission Linear" I Sound Vib. 503 p. 116113
- One-Way Electrical Transmission Lines," J. Sound Vib., **503**, p. 116113. [50] Liang, B., Guo, X., Tu, J., Zhang, D., and Cheng, J., 2010, "An Acoustic Rectifier," Nat. Mater., **9**(12), p. 989.
- [51] Li, X.-F., Ni, X., Feng, L., Lu, M.-H., He, C., and Chen, Y.-F., 2011, "Tunable Unidirectional Sound Propagation Through a Sonic-Crystal-Based Acoustic Diode," Phys. Rev. Lett., 106(8), p. 084301.
- [52] Boechler, N., Theocharis, G., and Daraio, C., 2011, "Bifurcation-Based Acoustic Switching and Rectification," Nat. Mater., 10(9), p. 665.
 [53] Ma, C., Parker, R. G., and Yellen, B. B., 2013, "Optimization of an Acoustic
- [53] Ma, C., Parker, R. G., and Yellen, B. B., 2013, "Optimization of an Acoustic Rectifier for Uni-directional Wave Propagation in Periodic Mass-Spring Lattices," J. Sound Vib., 332(20), pp. 4876–4894.
- [54] Moore, K. J., Bunyan, J., Tawfick, S., Gendelman, O. V., Li, S., Leamy, M., and Vakakis, A. F., 2018, "Nonreciprocity in the Dynamics of Coupled Oscillators With Nonlinearity, Asymmetry, and Scale Hierarchy," Phys. Rev. E, 97(1), p. 012219.
- [55] Bukhari, M., and Barry, O., 2022, "Substantial Frequency Conversion at Long-Wavelength Limit in Metamaterial With Weakly Nonlinear Local Electromechanical Resonators," Under review.
- [56] Bukhari, M. A., and Barry, O. R., 2020, "Electromechanical Diode: Acoustic Non-Reciprocity in Weakly Nonlinear Metamaterial With Electromechanical Resonators," ASME 2020 International Design Engineering Technical Conferences and Computers and Information in Engineering Conference, Online, Aug. 17, American Society of Mechanical Engineers.
- [57] Erturk, A., and Inman, D. J., 2011, Piezoelectric Energy Harvesting, John Wiley & Sons, New York.
- [58] Jiao, W., and Gonella, S., 2019, "Doubly Nonlinear Waveguides With Self-Switching Functionality Selection Capabilities," Phys. Rev. E, 99(4), p. 042206.
- [59] Fronk, M. D., and Leamy, M. J., 2017, "Higher-Order Dispersion, Stability, and Waveform Invariance in Nonlinear Monoatomic and Diatomic Systems," ASME J. Vib. Acoust., 139(5), p. 051003.
- [60] Jiao, W., and Gonella, S., 2021, "Wavenumber-Space Band Clipping in Nonlinear Periodic Structures," Proc. R. Soc. A, 477(2251), p. 20210052.
- [61] Bilal, O. R., Foehr, A., and Daraio, C., 2017, "Bistable Metamaterial for Switching and Cascading Elastic Vibrations," Proc. Natl. Acad. Sci. U.S.A., 114(18), pp. 4603–4606.
- [62] Yasuda, H., Buskohl, P. R., Gillman, A., Murphey, T. D., Stepney, S., Vaia, R. A., and Raney, J. R., 2021, "Mechanical Computing," Nature, 598(7879), pp. 39–48.

- [63] Mahboob, I., Flurin, E., Nishiguchi, K., Fujiwara, A., and Yamaguchi, H., 2011, "Interconnect-free Parallel Logic Circuits in a Single Mechanical Resonator," Nat. Commun., 2(1), pp. 1–7.
- [64] Zhang, T., Cheng, Y., Guo, J.-Z., Xu, J.-Y., and Liu, X.-J., 2015, "Acoustic Logic Gates and Boolean Operation Based on Self-Collimating Acoustic Beams," Appl. Phys. Lett., 106(11), p. 113503.
- [65] Zhu, S., Dreyer, T., Liebler, M., Riedlinger, R., Preminger, G. M., and Zhong, P., 2004, "Reduction of Tissue Injury in Shock-Wave Lithotripsy by Using an Acoustic Diode," Ultrasound Med. Biol., 30(5), pp. 675–682.
- [66] Maldovan, M., 2013, "Sound and Heat Revolutions in Phononics," Nature, 503(7475), pp. 209–217.
- [67] Li, B., 2010, "Now You Hear Me, Now You Don't," Nat. Mater., **9**(12), pp. 962–
- [68] Funayama, K., Tanaka, H., Hirotani, J., Shimaoka, K., Ohno, Y., and Tadokoro, Y., 2021, "Carbon Nanotube-Based Nanomechanical Receiver for Digital Data Transfer," ACS Appl. Nano Mater., 4(12), pp. 13041–13047.
- [69] Mohammadi, S., and Adibi, A., 2011, "On Chip Complex Signal Processing Devices Using Coupled Phononic Crystal Slab Resonators and Waveguides," AIP Adv., 1(4), p. 041903.
- [70] Zega, V., Silva, P. B., Geers, M. G., and Kouznetsova, V. G., 2020, "Experimental Proof of Emergent Subharmonic Attenuation Zones in a Nonlinear Locally Resonant Metamaterial," Sci. Rep., 10(1), pp. 1–11.